UNIVERSIDADE FEDERAL DE SÃO CARLOS
CENTRO DE CIÊNCIAS EXATAS E DE TECNOLOGIA
PROGRAMA DE PÓS-GRADUAÇÃO EM CIÊNCIA E ENGENHARIA DE MATERIAIS

EFFECT OF STRUCTURAL SINGULARITIES ON SUPERWETTABILITY OF SIO_2-BASED COATINGS

Lucas Daniel Chiba de Castro

São Carlos
2019

UNIVERSIDADE FEDERAL DE SÃO CARLOS
CENTRO DE CIÊNCIAS EXATAS E DE TECNOLOGIA
PROGRAMA DE PÓS-GRADUAÇÃO EM CIÊNCIA E ENGENHARIA DE MATERIAIS

EFFECT OF STRUCTURAL SINGULARITIES ON SUPERWETTABILITY OF SIO_2-BASED COATINGS

Lucas Daniel Chiba de Castro

Tese apresentada ao Programa de Pós-Graduação em Ciência e Engenharia de Materiais como requisito parcial à obtenção do título de DOUTOR EM CIÊNCIA E ENGENHARIA DE MATERIAIS

Orientador: Dr. Luiz Antonio Pessan
Coorientador: Dr. Nelson Marcos Larocca
Agência financiadora: FAPESP – Processo: 2015/20052-0

São Carlos
2019

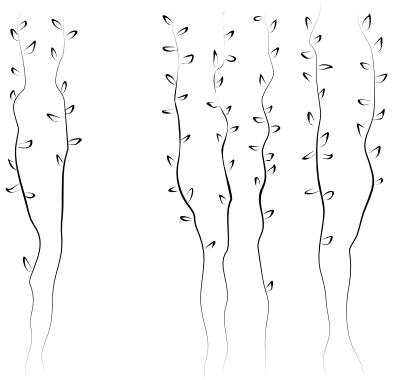

Just whispers in the wind…

VITAE OF THE CANDIDATE

Master’s degree in Materials Science and Engineering by UFSCar (2014)

Bachelor's degree in Materials Engineering by UFSCar (2011)

UNIVERSIDADE FEDERAL DE SÃO CARLOS

Centro de Ciências Exatas e de Tecnologia
Programa de Pós-Graduação em Ciência e Engenharia de Materiais

Folha de Aprovação

Assinaturas dos membros da comissão examinadora que avaliou e aprovou a Defesa de Tese de Doutorado do candidato Lucas Daniel Chiba de Castro, realizada em 07/11/2019:

Prof. Dr. Luiz Antonio Pessan
UFSCar

Prof. Dr. Leonardo Bresciani Canto
UFSCar

Prof. Dr. Luiz Henrique Capparelli Mattoso
EMBRAPA

Prof. Dr. André Rocha Studart
ETH Zurich

Prof. Dr. Celso Valentim Santilli
UNESP

Certifico que a defesa realizou-se com a participação à distância do(s) membro(s) André Rocha Studart e, depois das arguições e deliberações realizadas, o(s) participante(s) à distância está(ao) de acordo com o conteúdo do parecer da banca examinadora redigido neste relatório de defesa.

Prof. Dr. Luiz Antonio Pessan

ACKNOWLEDGEMENTS

To São Paulo Research Foundation (FAPESP) for the financial support under process number 2015/20052-0.

To Conselho Nacional de Desenvolvimento Científico e Tecnológico (CNPq) for the financial support under process number 163565/2014-7.

This study was financed in part by the Coordenação de Aperfeiçoamento de Pessoal de Nível Superior - Brasil (CAPES) - Finance Code 001

To all beloved people who made it happen.

To you, dear reader…

ABSTRACT

A detailed study on the correlation between structural singularities and wettability of neat and chemically modified coatings prepared from layer-by-layer (LbL) assembled silica nanoparticles (SiO_2) was performed. Nanoporous-driven superhydrophilicity of neat SiO_2-based coatings might not be mainly governed by thickness as usually reported in literature; instead, superficial homogeneity should be carefully considered and, if a uniform nanoporous structure is obtained, superhydrophilic behavior should be observed. Here, highly homogeneous structures were achieved by employing water-based dipping suspensions containing above 0.03 wt% of SiO_2 with 7nm and 22nm of diameter. Aiming the completely opposite wetting behavior, chemically modified hierarchical structures were prepared using two different approaches: random roughened surfaces were obtained by exploring stacking defects spontaneously arisen after 15, 30 and 45 assembly cycles of small SiO_2 particles; while a particular structure, commonly known as raspberry-like, was obtained by depositing small SiO_2 ("*berries"*) over the first deposited large SiO_2 (*"cores"*). As an intrinsic feature of the studied system, the average slope of random roughened surfaces seems to be constant and virtually independent of the number of deposited layers. Additionally, the local slopes were always lower than a critical value (Φ_{crit}) required to stabilize the solid-liquid-air interface, therefore, and a fully wetted Wenzel state with water contact angle (WCA) of approximately 130º was invariably observed. On the other hand, since the local slopes of the raspberry-like structure follow a nearly spherical curvature, small SiO_2 can stabilize the solid-liquid-air interface by increasing the local contact angle and avoiding the deep penetration of water into the surface asperities. For the studied conditions, WCA as large as 167º was observed. The small berries might also play an important role in the pinning effect of the solid-liquid-air contact line, bringing to life the phenomena so-called *Lotus Effect.*

Keywords: SiO_2; superhydrophilic; superhydrophobic; layer-by-layer; coating; Lotus Effect

RESUMO

EFEITO DE SINGULARIDADES ESTRUTURAIS NA SUPERMOLHABILIDADE DE REVESTIMENTOS BASEADOS EM SiO_2

Investigou-se a correlação entre singularidades estruturais e molhabilidade de revestimentos puros e quimicamente modificados, baseados em nanopartículas de sílica (SiO_2) preparados por layer-by-layer (LbL). A superhidrofilia de revestimentos puros induzida por nanoporosidade pode não ser primariamente regida pela espessura, conforme descrito na literatura; acredita-se que a homogeneidade superficial também deve ser considerada e, caso uma estrutura nanoporosa uniforme seja obtida, o efeito superhidrofílico potencialmente será observado. Neste estudo, revestimentos uniformes foram obtidos através do emprego de suspensões a base d'água contendo acima de 0,03% em massa de SiO_2 de 7nm e 22nm de diâmetro. Visando o efeito de molhabilidade oposto, estruturas hierárquicas quimicamente modificadas foram preparadas por duas abordagens distintas: superfícies de rugosidade aleatória foram obtidas através de defeitos manifestados espontaneamente após 15, 30 e 45 ciclos de deposição de SiO_2 pequenas; por outro lado, uma estrutura peculiar denominada *raspberry,* foi obtida através da deposição de SiO_2 pequenas (*"berries"*) sobre SiO_2 grandes (*"cores"*). Observou-se que o declive médio das superfícies com rugosidade aleatória é virtualmente constante e independente do número de camadas depositadas. Adicionalmente, o declive local é sempre menor do que um valor crítico (Φ_{crit}) necessário para estabilizar a interface sólido-líquido-ar e, portanto, um ângulo de contato com a água (WCA) de aproximadamente 130º é invariavelmente observado. Em contrapartida, uma vez que o declive local de estruturas *raspberry* segue uma curvatura quase esférica, SiO_2 pequenas estabilizam a interface solido-líquido-ar através do aumento do ângulo de contato local, evitando a penetração de água nas asperidades da superfície. Para as condições estudadas, um WCA de aproximadamente 167º foi observado. As SiO_2 pequenas ainda promovem o efeito de *pinning* da linha de contato solido-líquido-ar, dando origem ao fenômeno denominado *Efeito Lótus.*

Palavras-chave: SiO_2; superhidrofilia; superhidrofobia; layer-by-layer; revestimentos; Efeito Lótus

PUBLICATIONS

CASTRO, L.D.C.; LAROCCA, N.M.; PESSAN, L.A. Towards the development of superhydrophilic SiO_2-based nanoporous coatings: Concentration and particle size effect. THIN SOLID FILMS, v. 651, p. 138-144, 2018.

CASTRO, L.D.C.; LAROCCA, N. M.; SANTOS, L. M. A.; PESSAN, L.A. Desenvolvimento de Revestimentos Superhidrofílicos Nanoestruturados por Deposição Layer-by-Layer. In: 14º CONGRESSO BRASILEIRO DE POLÍMEROS. Anais do Congresso. Águas de Lindóia – SP. Outubro, 2017.

x

INDEX

TABLE OF TABLES

Page

TABLE OF FIGURES

Page

1 INTRODUCTION

It is undeniable that bioinspired and biomimetic terms have their spot among the trendiest topics in the scientific community. However, despite the complexity of biological structures, the motivation is always straight and clear: providing elegant solutions inspired by Mother Nature for humankind problems.

Wettability is central to numerous biological processes and, nowadays, to many engineering and industrial technologies. However, after a quick research, one will promptly realize that the humankind fascination with water-spreading mechanisms is not *something new.* Wetting can be defined as the ability of a liquid to maintain contact with a solid surface and is ruled by the intermolecular interactions between the two phases [1–3] . Research on wetting and wettability can be traced back to over 200 years ago, when the pioneer Thomas Young proposed the concept of contact angle of a liquid to establish the notion of surface wettability in 1805 [4].

Irving Langmuir, Nobel Laureate for surface chemistry in 1932, reported in 1920 that an absorbed monolayer of an organic compound could dramatically affect the frictional and wetting properties of solid surfaces [5]. This finding led to the widespread use of chemical modification to control the surface wetting behavior. However, the interest in fine-tuning wettability of solids was particularly intensified after a wide acceptance that liquid spread control can be achieved through the manipulation of both surface roughness and chemistry [6,7], resulting in superwetting phenomena.

The theoretical framework that still governs surface science was developed in the mid-twentieth. In 1936, Wenzel [8] suggested that it is possible to boost the intrinsic wetting behavior of a solid surface by introducing roughness at the right scale. In 1944, Cassie and Baxter [9] extended such concept to a particular situation in which air can be trapped in between the water and solid phases.

Superhydrophobic surfaces refer to those on water contact angle WCA ≥ 150º, however, despite few examples, the development of water-repellent materials has been delayed due to the lack of fundamental principles [7].

In 1997, Barthlott and Neinhuis [10] demonstrated that the interdependence between surface roughness, reduced particle adhesion and water repellency is the keystone in the self-cleaning mechanism of many biological surfaces. Among them, it is highlighted *Nelumbo nucifera,* popularly known as Lotus flower (Figure 1.1). When water falls upon a Lotus leaf it is observed the formation of high contact angle drops that can easily roll off from the surface, removing impurities along their pathway. This remarkable phenomenon is manifested by superhydrophobic features and deservedly entitled as *lotus effect*. In 2002 it was demonstrated for the first time the crucial role of multiscale structures in the superhydrophobicity; therefore, the lotus effect is dependent on the perfect synergy between the micro/nano hierarchical roughness and low surface energy [11]. In this way, revealing the mechanism of extremely water repellent examples in nature enabled a totally innovative biomimetic approach to design superhydrophobic surfaces.

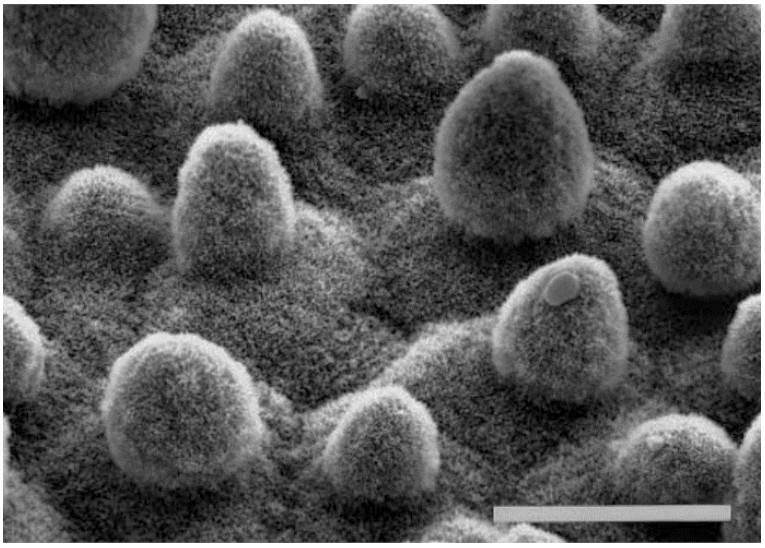

Figure 1.1 - Scanning electron micrograph (SEM) of top surface of the Nelumbo nucifera leaf. Scale bar: 20 µm. Adapted from [10].

On the other extreme, *superhydrophilicity*, which received relatively little research interest before the 1990s, gained notoriety soon after the explosion of research on superhydrophobic surfaces. Despite of some divergences, superhydrophilic surfaces are normally described on which WCA ≤ 5° within 0.5s

or less. Such strong affinity with water is responsible for the antifogging effect, which may prevent light scattering of transparent substrates by the almost instantaneous spreading of condensed water droplets [12–14]. Regarding the preparation of superhydrophilic surfaces, two basic strategies have been employed. The first is based on the use of photochemically active materials such as titanium dioxide (TiO_2) that exhibit superhydrophilicity after exposure to UV or, with proper chemical treatments, visible radiation. However, although much progress has been made, TiO_2-based coatings typically lose their super-wetting properties when placed in dark environment, been limited to outdoor applications [15–18]. The second, and more recent, approach involves the use of texturized surfaces to induce superwetting behavior through the principles described by Wenzel [8]. It was demonstrated that both lithographically textured and micro/nanostructured surfaces might exhibit superhydrophilicity, if roughness is introduced at the right scale [19–22].

As a consequence, superhydrophobicity and superhydrophilicity secured their spot among the trendiest topics concerning the wetting field; in which efforts have been directed to elucidate the correlation between liquid penetrating and/or suspending on phenomena with complex topographies, often controlled at sub-microscopic level [22–26].

At this point it is important to express that the present work was initially designed to propose a novel and inexpensive method to induce and control the superwettability of solids just by tuning their topography and surface chemistry.

However, as any organic structure, the project matured and evolved over the years. Therefore, in a more realistic way, this study is focused on the development of neat and chemically modified silica nanoparticles (SiO_2) coatings prepared via layer-by-layer assembly technique (LbL). Taking advantage of the nanometric control of LbL process, specific topographies were carefully tailored in order to advance a small step towards elucidating some concepts of (super)wettability that, still nowadays, are not totally understood.

4

2 OBJECTIVES

The objectives of this study were to tailor specific topographies of neat and chemically modified SiO_2-based coatings in order to induce different water-spreading mechanisms and discuss some concepts that, even over 200 years of wettability research field, are still not a consensus among the academic community.

Additionally, as a specific objective of the present work, it was investigated the utility of layer-by-layer (LbL) process conducted by *dip-coating* in the preparation of functional superhydrophilic and superhydrophobic surfaces through the manipulation of processing variables such as particle size, concentration of dipping suspensions and number of assembly cycles.

6

3 LITERATURE REVIEW

3.1 Nature as a source of inspiration

After billions of years of evolution, nature creates a countless variety of fantastic natural materials, featuring a wide range of properties. In the last decades, with the development of advanced physical characterization techniques, Mother Nature has given away some of her secrets and a new class of bioinspired and biomimetic materials stole the spotlight, attracting attention from the academic community.

Concerning wettability, the most famous natural example is undoubtedly the Lotus Flower. As a symbol of purity in many cultures, lotus leaf is famous for its low-adhesive superhydrophobicity and self-cleaning property. Superhydrophobicity of lotus leaves results from their intrinsic hierarchical surface structure, constituted by randomly oriented nano-scale hydrophobic wax tubules on the top of micro-scale convex cell papillae (Figure 3.1a) [10,27].

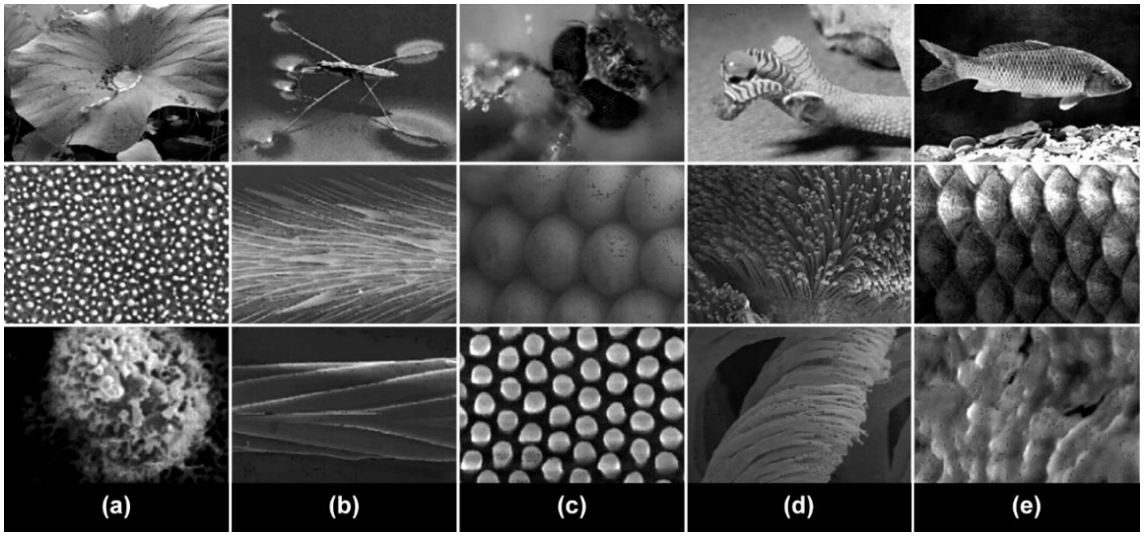

Figure 3.1 - Typical biological materials with superwettability and corresponding multiscale structures. (a) Lotus leaves; (b) water strider legs; (c) mosquito compound eyes (d) gecko foot and (e) fish scales. Adapted from [2].

However, researchers have disclosed many other functional biological interfacial materials such as the durable and robust superhydrophobic water

strider leg (Figure 3.1b); the superhydrophobic, antifogging, and antireflective mosquito compound eye (Figure 3.1c); the superhydrophobic, reversible adhesive and self-cleaning gecko feet (Figure 3.1d); and the superoleophilic in air, superoleophobic in water and drag reduction fish scale (Figure 3.1e).

3.2 Wettability from the very first beginning

Wettability of solids is ruled by the synergy between surface chemistry and surface roughness. In general, water contact angle (WCA) is applied to evaluate the static wettability of a solid surface, while the sliding angle (SA) or CA hysteresis (difference between advancing and receding angles) are considered while describing its dynamic wetting behavior. Traditionally hydrophilic surfaces exhibit WCAs θ_e < 90° and, intuitively, those that have WCAs θ_e > 90° are hydrophobic, as shown in Figure 3.2.

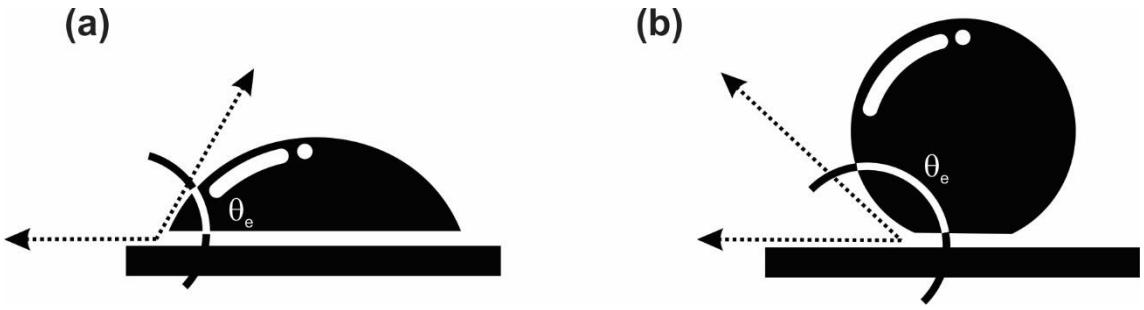

Figure 3.2 - Wettability of (a) hydrophilic and (b) hydrophobic surfaces.

Such concept originated from Young's equation, in which 90° is considered as the mathematical threshold that categorizes the wettability of a given surface [28]. Later on, a lower boundary of around 65° was proposed by considering the interphase water molecular interactions and structures [29–31]. However, at least for now, let's stick to the acclaimed and well-established theory. By Young's equation:

$$\cos\theta_e = \frac{\gamma_{SA} - \gamma_{SL}}{\gamma_{LA}} \tag{3.1}$$

where θ_e is the intrinsic WCA of the material; γ_{SA}, γ_{SL} and γ_{LA} are, respectively, the solid-air, solid-liquid and liquid-air interface tensions.

It is important to note that Young's model is ideal and can just be applied on perfectly smooth and chemically homogeneous surfaces. The surface roughness contribution was posteriorly introduced by the Wenzel and Cassie-Baxter models.

3.3 Wenzel and Cassie-Baxter models

In 1936, Wenzel proposed a first approach to introduce the influence of surface roughness on wettability of solids [8]. The apparent contact angle θ_e^w on a rough surface can be estimated by considering a small displacement dx of the contact line along the parallel direction of the surface, as shown in Figure 3.3 [32]. Then, the total free energy difference dF is given by:

$$dF = r(\gamma_{SL} - \gamma_{SA})dx + \gamma_{LA}dx\cos\theta_e^W \tag{3.2}$$

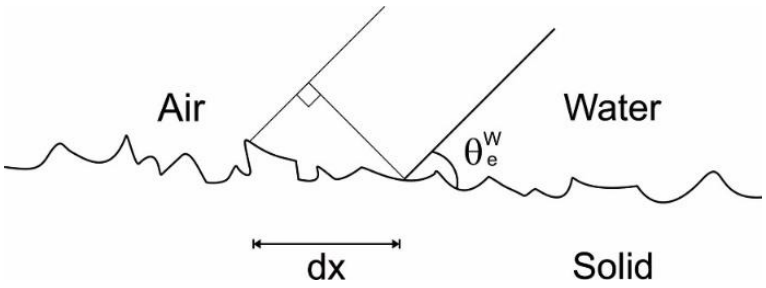

Figure 3.3 - Infinitesimal spreading of a water droplet on a rough surface

where and r is the roughness factor, defined as the ratio of the actual surface area to the projected surface area. The equilibrium condition is given by the minimum of F, from which the Wenzel's equation is obtained:

$$\cos\theta_e^w = \mathrm{r}\cos\theta_e \tag{3.3}$$

where θ_e is the intrinsic contact angle as measured on a smooth surface.

According to Equation (3.3) , if the liquid completely fills the grooves of a solid surface as shown in Figure 3.4a, increasing the surface roughness might enhance its hydrophilicity or hydrophobicity, depending on the intrinsic wettability of the material. In other words, for a rough surface r is always larger than 1; therefore, by increasing the roughness factor, a hydrophilic surface would be more hydrophilic while a hydrophobic surface would be more hydrophobic.

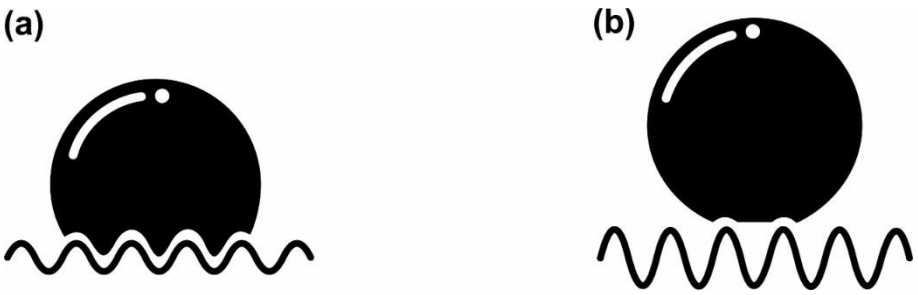

Figure 3.4 - Wetting models proposed by (a) Wenzel and (b) Cassie-Baxter

If θ_e > 90°, the surface energy of the dry solid is lower compared to the wet solid ($\gamma_{SA} < \gamma_{SL}$) and thereby, the contact line might not follow the surface profile as supposed by the Wenzel regime. Moreover, it can be energetically favorable for a water droplet to bridge across the surface asperities, resulting in a composite surface with air pockets trapped within the structure as exhibited by Figure 3.4b. In this case, displacing the contact line of a quantity dx parallel to the surface implies in a change of free energy dF equal to [32]:

$$dF = f_s(\gamma_{SL} - \gamma_{SA})dx + (1 - f_s)\,\gamma_{LA}dx + \gamma_{LA}dx\cos\theta_e^{CB} \tag{3.4}$$

where θ_e^{CB} is the Cassie-Baxter apparent contact angle; and f_s is the solid fraction. At the equilibrium F is minimum, thus:

$$\cos\theta_e^{CB} = f_s\cos\theta_e + f_s - 1 \tag{3.5}$$

Equation (3.5) is a particular form of the Cassie-Baxter model [9], which estimates the contact angle for a drop deposited on a composite surface. The

$\cos\theta_e^{CB}$ is obtained by the average of the cosines of the intrinsic WCA with solid and air, weighted by their respective surface fraction.

Despite some mathematical similarities, there is a fundamental difference between the two models. Even though both hydrophilic and hydrophobic phenomenon can be manifested in Wenzel regime, the water droplets pin the surface in a wet-contact mode and high CA hysteresis is invariably observed. In the Cassie-Baxter regime, hydrophobic by definition, water droplets adopt a non-wetted-contact mode and can easily roll off owning to the low adhesive force [33]

Concerning specifically superhydrophobic surfaces, Wang and Jiang [34] suggest the existence of five different wetting states: the aforementioned Wenzel's and Cassie's states; the transitional state between the Wenzel's and Cassie's state; and two particular cases of Cassie's regime so-called the *Lotus state* (surfaces with micro- nanoscale structures and ultralow adhesion to liquids) and the *Gecko state* (rough surfaces with high adhesion to liquids). Notwithstanding each superwetting state has its own particularities and importance on fundamental research and technological applications, the current studies are mainly focused on the preparation of surfaces in Lotus state due to their attractive self-cleaning features. However, even in such trendy topic, conceptual divergences are still a constant among the academic community.

3.4 Induced superwettability and the topographic control

At this point the reader should be aware that a WCA of 0° cannot be achieved from a flat homogeneous surface. On the other hand, even after proper chemical modification with hydrophobic fluorides, the maximized WCA on flat surfaces is around 118° [2]. In this way, the topographic control might be a suitable (not to say mandatory) strategy to induce superwettability on solids.

Indeed, among the innumerous examples, some particularly elegant methods have been proposed for imparting surface roughness to substrates such as controlled crystallization [35,36], phase separation [37–40], chemical vapor deposition [41–43], electrospinning [44–47] and bioinspired morphogenesis [48]. However, despite of this author's personal enthusiasm for the endless

possibilities, the wisest option is to focus in one approach at a time. Therefore, this study was based on the surface manipulation of neat and chemically modified silica nanoparticles (SiO_2) coatings prepared via layer-by-layer assembly technique.

Electrostatic layer-by-layer assembly (LbL) is a versatile technique based on the alternated adsorption of oppositely charged components on solid substrates to build-up ultrathin multilayer films. Although LbL assembly can be dated back to the pioneering work of Iler in 1966 [49], its importance was not recognized until the early 1990s, when it was rediscovered by Decher and co-workers [50].

3.5 The LbL approach

The process of sequential adsorption of monolayers is graphically described in Figure 3.5, exemplifying the adsorption of anionic and cationic polyelectrolytes with identical charges at each end.

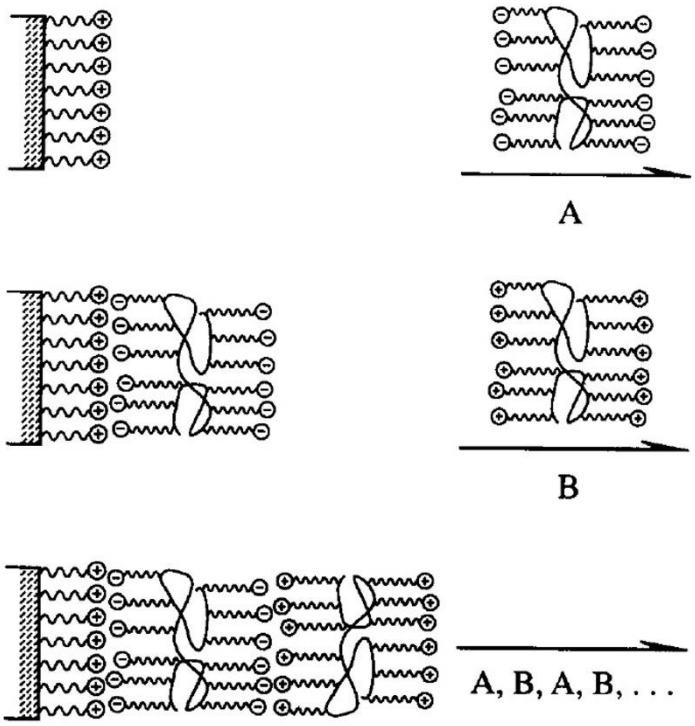

Figure 3.5 - Schematic illustration of the adsorption process. Adapted from [51].

In step A, a positively charged substrate is immersed in the solution of the negatively charged polyelectrolyte leading to the adsorption of one monolayer and to the reversal of the surface charge. Then the substrate is rinsed in pure water in order to remove the non-adsorbed component. In step B, the substrate is dipped into the solution containing the positively charged polyelectrolyte. Again, a monolayer is adsorbed but now the original positive surface charge is restored. After a second rinsing step the process can be carried out in a cyclic fashion, enabling multilayer assemblies (A, B, A, B…).

If the rinsing steps are omitted, an adhering layer of one solution would be left on the surface of the substrate. This would lead to a contamination of the next solution and, eventually, to the co-precipitation of both compounds and incorporation of precipitated particles into the following layer.

Such process of multilayer formation is based on the attraction of opposite charges, and thus requires a minimum of two oppositely charged molecules. However, one can incorporate more than two molecules into the multilayer, simply by immersing the substrate in as many solutions as desired, as long as the charge is reversed from layer to layer. Additionally, the immersion procedure poses no restrictions neither to the size of the substrate nor to the automatization in a continuous process [50]. Despite the LbL concept was exemplified for polyelectrolytes, it can be extended to oppositely charged inorganic nanoparticles, macromolecules or even supramolecular systems [52] and, among several applications, employed in the topographic control of solids.

3.5.1 Superhydrophilicity

Taking advantage of the versatility of LbL technique, surface morphology can be manipulated by controlling simple materials and processing parameters. Liu and He [53] prepared antireflective (AR) superhydrophilic coatings based on SiO_2 nanoparticles of 30 nm (S-30), 150 nm (S-150) and polyelectrolytes via layer-by-layer assembly with postcalcination. Multifunctional properties can be achieved by employing layers of differently sized nanoparticles. In the optimal condition, an S-30 underlayer contributes to the increase of transmittance while

the subsequently adsorbed S-150 and S-30 nanoparticles are responsible for the enhanced surface roughness, thus, superhydrophilicity.

Zhang et al [54] presented a method for the preparation of AR and antifogging coatings by LbL deposition of mesoporous silica ($MSiO_2$) nanoparticles and poly(diallyldimethylammonium chloride) (PDDA). Both features were attributed to the loose stacking of $MSiO_2$/PDDA multilayers allied to the intrinsic porosity of the $MSiO_2$, which greatly increased the surface roughness and enabled the fabrication of superhydrophilic coatings with low refractive index. Using a similar approach, Xu and He [55] prepared superhydrophilic coatings onto PMMA and glass substrates by integrating solid and mesoporous SiO_2 nanoparticles without any post-treatments.

Geng and coworkers [56] prepared highly transparent superhydrophilic SiO_2-based coatings onto poly(methyl methacrylate) (PMMA) substrates via LbL assembly followed by oxygen plasma treatment. By adjusting the number of deposited layers, surface roughness and internal structure can be tailored to achieve self-cleaning and AR properties (Figure 3.6).

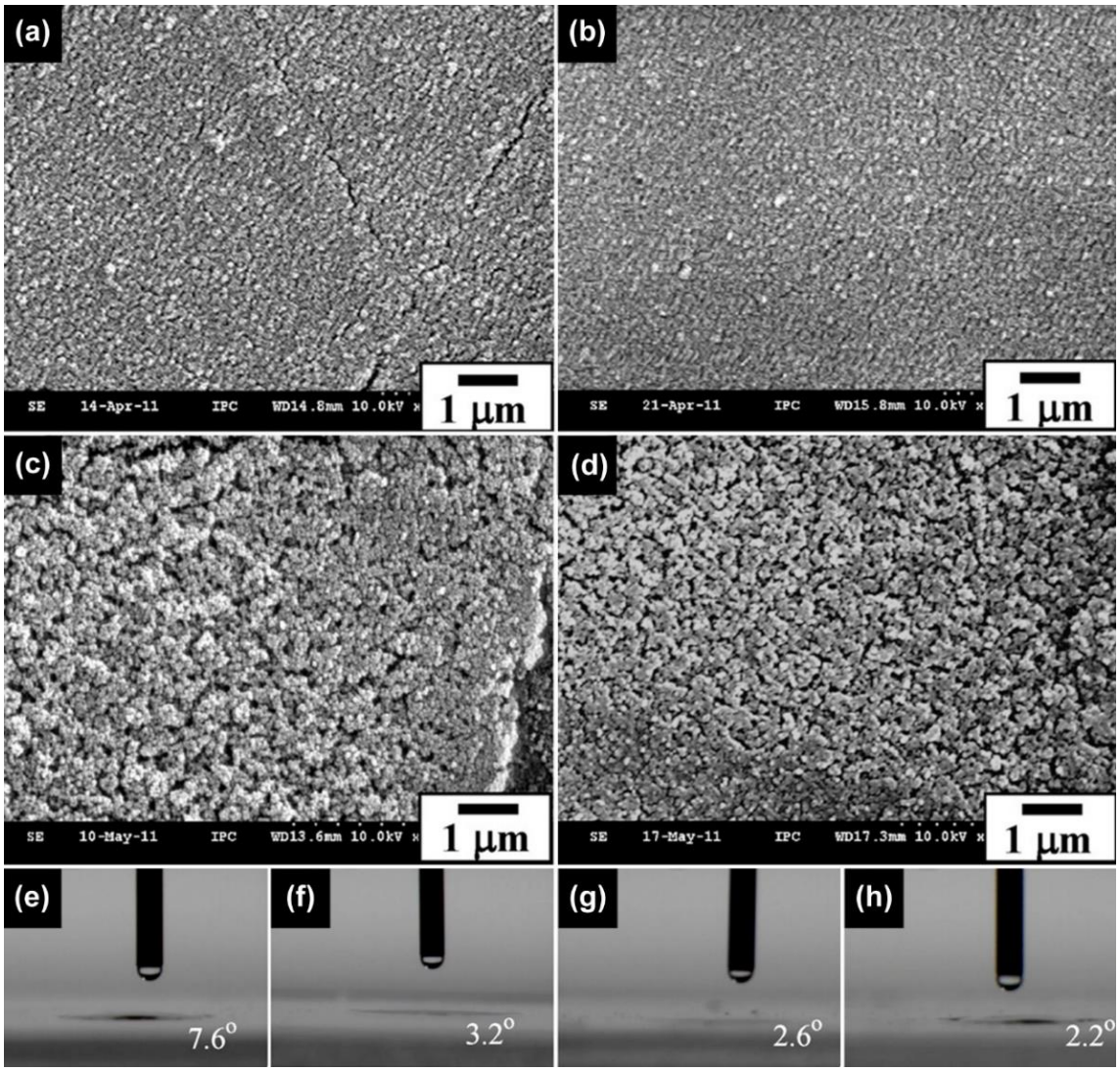

Figure 3.6 - SEM images of SiO_2-based coatings and their respective WCAs with (a and e) 9; (b and f) 10; (c and g) 11; (d and h) 13 deposited bilayers. Adapted from [56].

Guo et al. [57] described the fabrication of superhydrophilic coatings via LbL assembly onto quartz or glass slide substrate of poly(ethyleneimine)/poly(sodium 4-styrenesulfonate) (PEI/PSS) with *in-situ* formation of calcium silicate hydrates (CSH). It was found that surface morphology Figure 3.7a-c, roughness and thickness can be tuned by the number of deposition cycles and initial concentration of assembly solutions to effectively control the hydrophilicity Figure 3.7d.

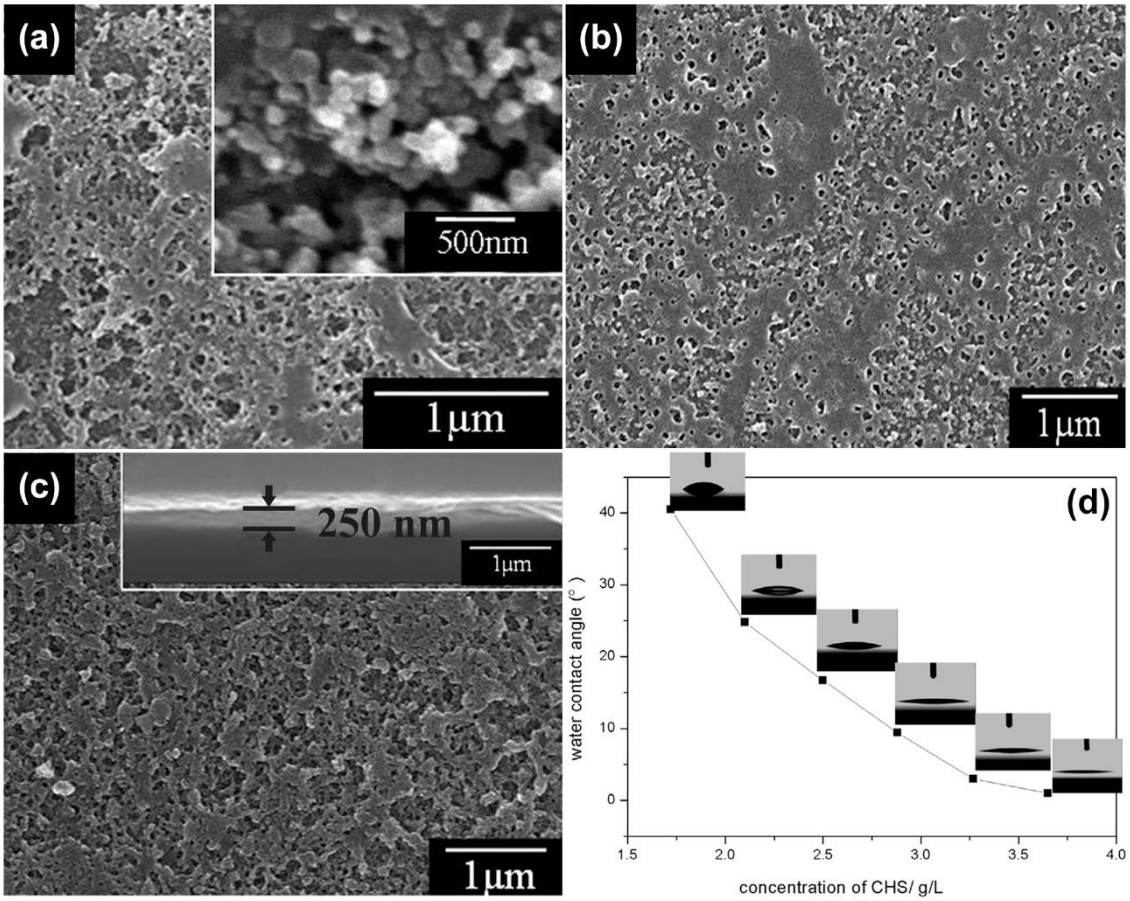

Figure 3.7 - SEM micrographs of (PEI/PSS–CSH) coatings prepared with (a) one; (b) two; and (c) three deposition cycles. (d) The variation of contact angles induced by the various concentration of CSH for the coating shown in (c). Adapted from [57].

In an eco-friendly approach, Choi and coworkers [58] developed highly transparent superhydrophilic coatings through the electrostatic interaction- or hydrogen-bonding-based LbL assembly of the biotic materials chitosan and rice husk ash nanosilica. The as-prepared multilayer coatings have rough surface structures at the micro- nanoscale and, even under aggressive conditions, show excellent antifogging, anti-frosting and antibiofouling properties.

3.5.2 Superhydrophobicity

Naturally the LbL technique is not exclusively employed in the preparation of superhydrophilic surfaces. Probably the majority of the studies concerning the wetting field are focused on the charming superhydrophobic effect. Zhai et al. [59] demonstrated that the water-repellent behavior of the lotus leaf can be mimicked by creating a honeycomb-like polyelectrolyte multilayer structures overcoated with SiO_2 nanoparticles and modified by chemical vapor deposition (CVD) of a semifluorinated silane. Soeno and coworkers [60] prepared ultra-water-repellent surfaces via LbL assembly of poly(allylamine hydrochloride) (PAH), poly(acrylic acid) (PAA) and differently-sized SiO_2 nanoparticles followed by calcination. The obtained coatings have very complicated surface structures and, after chemical treatment with dichlorodimethylsilane, exhibit WCA larger than 160º (Figure 3.8a). The superhydrophobic behavior is attributed to the nanoscale roughness (Figure 3.8b) which may be tuned to control the surface wettability.

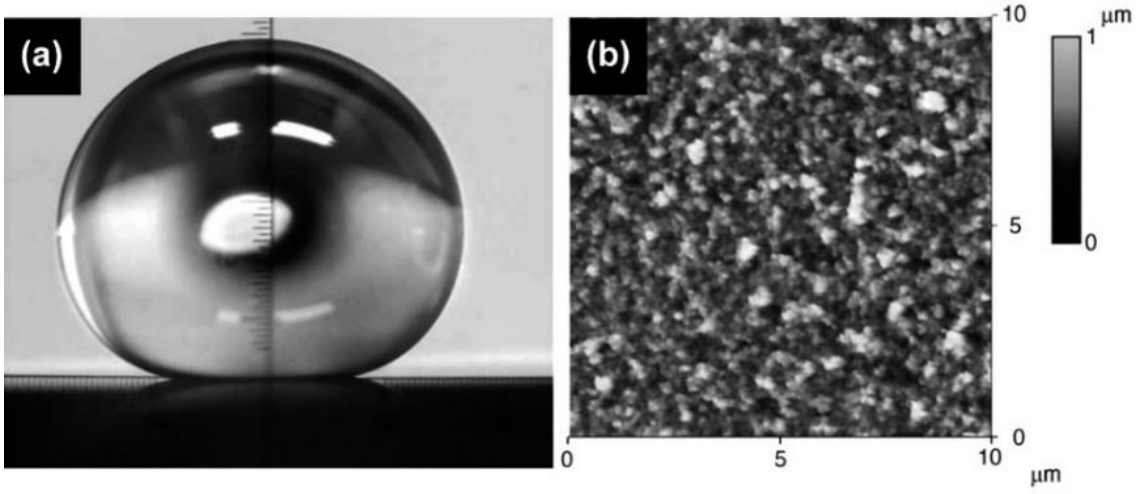

Figure 3.8 - (a) Photograph of a water droplet and (b) AFM image of the hydrophobic SiO_2 nanoparticle film. Adapter from [60].

Zhang et al. [61] demonstrated that PDDA-sodium silicate complexes (noted as PDDA-silicate) could be LbL assembled with PAA to produce mechanically stable antireflective and antifogging coatings. Later on, Li et al. [62] described the fabrication of antireflective superhydrophobic surfaces via LbL

deposition of PAH/SiO_2 multilayers followed by calcination and CVD of fluoroalkylsilane, onto the previously prepared PDDA-silicate/PAA films. It was found that the first-deposited silicate nanoporous layers are responsible for the AR effect, while the chemically modified rough SiO_2 coating acts as the water-repellent surface.

An inventive self-templated etching strategy was proposed to directly convert SiO_2 nanospheres into surface-rough SiO_2 (SR-SiO_2) nanoparticles by reaction with sodium borohydride ($NaBH_4$) [63]. The size of asperities on the nanoparticles surface can be tailored by carefully regulating the reaction time (Figure 3.9 a-b).

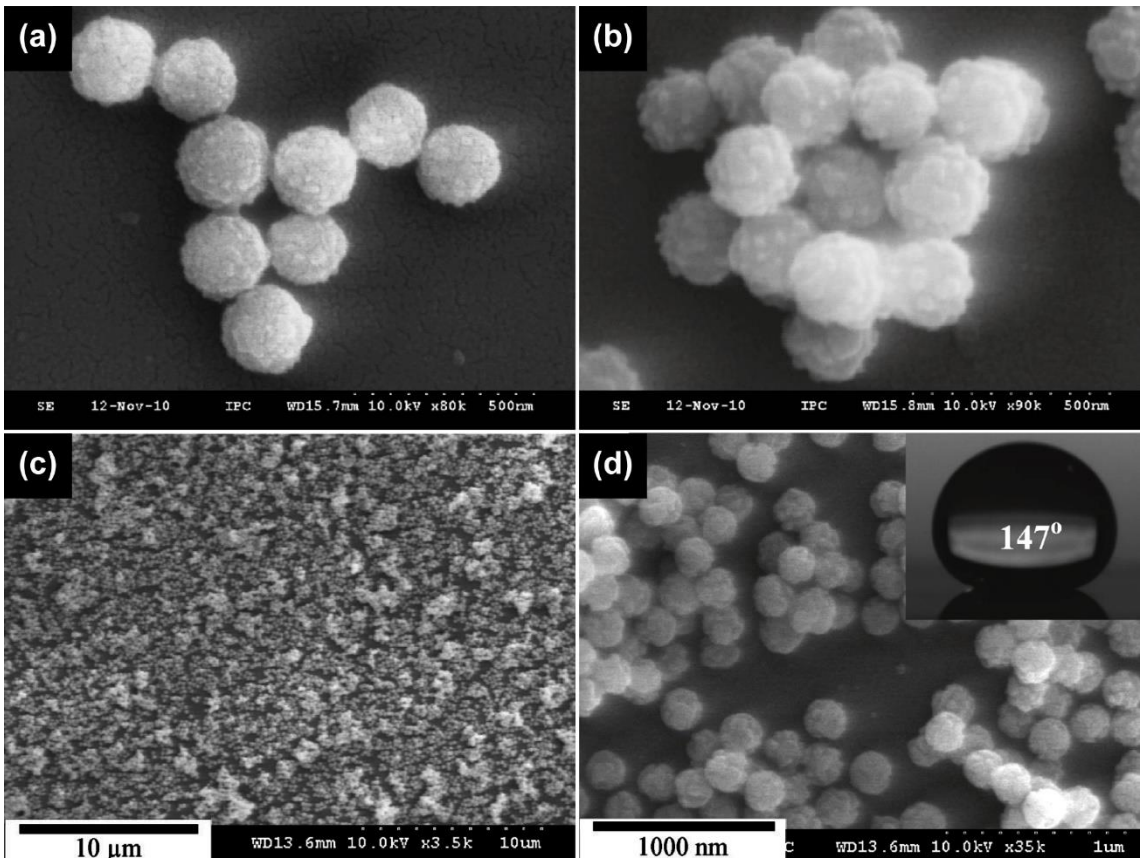

Figure 3.9 - SEM images of SR-SiO_2 obtained by etching SiO_2 nanospheres with NaBH4 for (a) 3h and (b) 4h; (c) and (d) particulate coating prepared using two deposition cycles. Adapted from [63].

After proper parameter refinement, SR-SiO_2 were employed as building blocks to construct particulate coatings on glass substrates via LbL assembly with

polyelectrolytes. According to the authors, two layers of SR-SiO_2 followed by calcination and modification by CVD of perfluorooctyltriethoxysilane (POTS) were enough to promote superhydrophobicity (Figure 3.9c-d).

As an alternative to the usage of polyelectrolytes, Zhang and coworkers [64] prepared superhydrophobic surfaces from negatively charged SiO_2 nanoparticles and a positively charged ionic liquid (IL) via LbL assembly. In virtue of the roughness produced by SiO_2, allied to the intrinsic low surface energy of the IL, the hybrid coatings achieved superhydrophobicity without posterior chemical modification.

3.5.3 Superwettability of SiO_2-based systems

It might sound a little bit repetitive and, actually, it really is. However, the presented studies were carefully selected to emphasize that, even being completely opposite wetting phenomena, superhydrophilicity and superhydrophobicity are intimately connected by the same key concept: the synergy between surface roughness and chemistry. At this point, it is important to summarize the current background.

While working with SiO_2-based system, surface chemistry can be easily modified with the aid of silanes; therefore, as the reader probably realized, the real challenge is precisely laid on the control of structural features.

As earlier discussed, studies have reported the utility of LbL assembly in the preparation of nanostructured coatings which, with optimized conditions, have the potential to be employed in the manufacturing process of superwetting surfaces. Nevertheless, it seems to be a consensus that the relation between processing parameters, structure and performance of coatings is still not completely understood and need to be systematically investigated for each individual system. So, metaphorically speaking, superhydrophilicity and superhydrophobicity seem to be *two sides of the same coin*, but do we really know their singularities?

4 MATERIALS AND METHODS

4.1 Materials

Poly(diallyldimethylammonium chloride) (PDDA, Mw = 200000 – 350000, 20 wt% aqueous solution); poly(acrylic acid) (PAA, Mw = 250000, 35 wt% aqueous solution); colloidal silica nanoparticles Ludox® SM (30 wt% SiO_2 suspension in water, 7nm average diameter); Ludox® TM-40 (40 wt% SiO_2 suspension in water, 22nm average diameter); trichlorododecylsilane ≥ 95.0% (GC); tetraethyl orthosilicate (TEOS, 99%); ammonium hydroxide solution (NH_4OH, ≥ 25% NH_3 in H_2O) and ethanol absolute (EtOH, 99.8%) were purchased from Sigma-Aldrich. Standard microscope glass slides were employed as substrates. Deionized water purified in a Millipore Milli-Q® system was exclusively used in all aqueous solutions and rinsing procedures. All reactants were used without further purification and their chemical structure are shown in Figure 4.1.

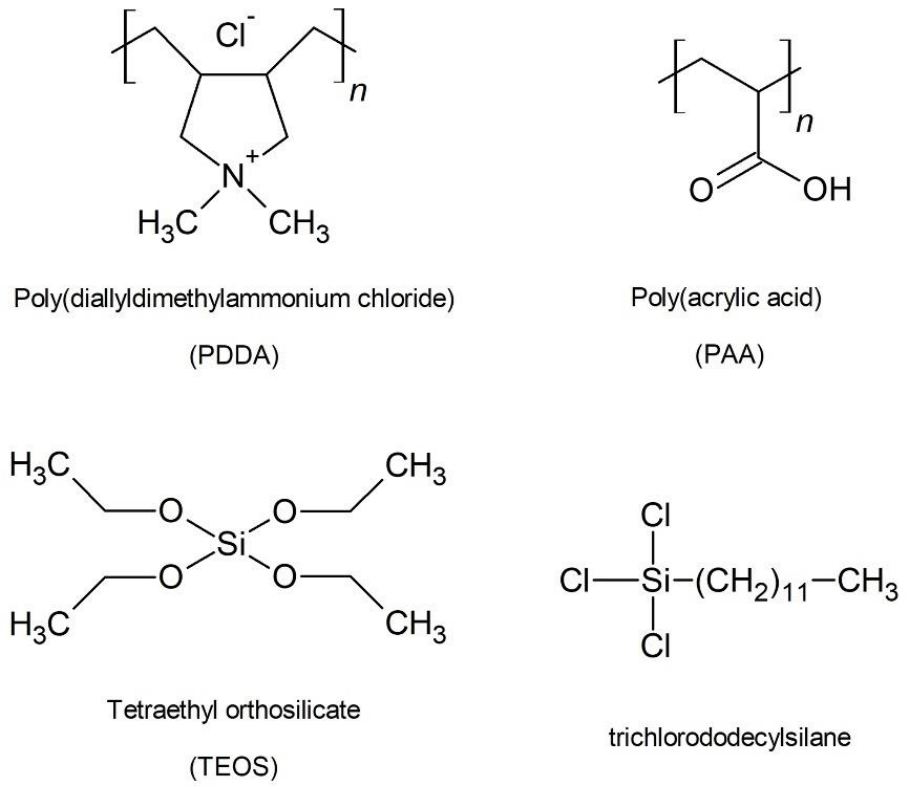

Figure 4.1 - Chemical structures of the reactants.

4.2 Methods

4.2.1 Synthesis of large SiO_2 nanoparticles

Stöber process [65] is a versatile sol-gel technique to prepare monodispersed SiO_2 spherical particles through hydrolysis and condensation reactions of TEOS in the presence of EtOH and NH_4OH. Homemade large SiO_2 nanoparticles with an average diameter of approximately 400nm were prepared by an adapted procedure based on previous studies [66–69].

Briefly, ultrapure water and NH_4OH were pre-mixed with EtOH for 5 minutes before the addition of TEOS. The reaction was conducted under vigorous stirring in a closed polyethylene reactor for 3h at room temperature. The suspension obtained was centrifuged at 10000 RPM, washed/re-dispersed 3 times in deionized water and dried in vacuum at 80°C overnight. The volumes of reactants employed in each synthesis batch are listed in Table 4.1.

Table 4.1 - Volumes of the reactants employed in the synthesis process

Reactant	Volume* (mL)
Water	9.0
NH_4OH	25.0
TEOS	3.1

**per 50ml of EtOH*

4.2.2 Multilayer assembly process

Prior to the deposition process, glass substrates were immersed in piranha solution (3:1 98% H_2SO_4:30% H_2O_2 mixture) for 20 min, rinsed with copious amount of water and dried under nitrogen (N_2) flow. *Warning: piranha solution reacts violently with organic materials and should be handled carefully*.

The deposition process consists of the alternated immersion of substrates into different aqueous solutions through a process commonly known as *dip-coating*. Sequential adsorption of multilayer coatings was performed in freshly cleaned glass slides assisted by an automated home-built dipping unit.

Immersion time for all polymers and nanoparticle suspensions was fixed in 15 min. Each deposition step was followed by a rinse step of 2 min to remove the non-adsorbed material on surface. In order to avoid cross-contamination, dipping solutions were renewed every 15 deposition cycles. The pH ~ 9, adjusted for all dipping solutions, was defined by attenuated total reflection-Fourier transform infrared spectroscopy and zeta potential analysis *(to be discussed)*.

The prepared coatings are composed of two main blocks. First, *adhesion layers* were used to improve binding of the polymer-nanoparticle system to the substrate. In this stage, two (PDDA/PAA) bilayers were deposited, in which PDDA (0.1 wt%) is the polycation and PAA (0.1 wt%) is the polyanion.

For the (PDDA/SiO_2) *body layers*, PDDA (0.1 wt%) was once more selected as the cationic solution while aqueous suspensions of the differently sized SiO_2 (0.01; 0.03; 0.05 and 0.1 wt%) were employed as the anionic component. In a first moment, the samples were identified as following: (PDDA/SiO_2 (x) y%)$_n$, where x refers to the SiO_2 size in nanometers, y refers to the concentration in weight of the SiO_2 aqueous suspension and n is the number of deposited bilayers. Nevertheless, as soon as the structures become more sophisticated, such notation will be updated and, naturally, the reader will be aware in advance.

The as-prepared coatings were dried at room temperature and calcinated at 500 °C for 4 h. Calcination step is responsible for removing the organic part and enhancing mechanical stability through formation of siloxane bridges. The employed procedure is schematically illustrated on Figure 4.2.

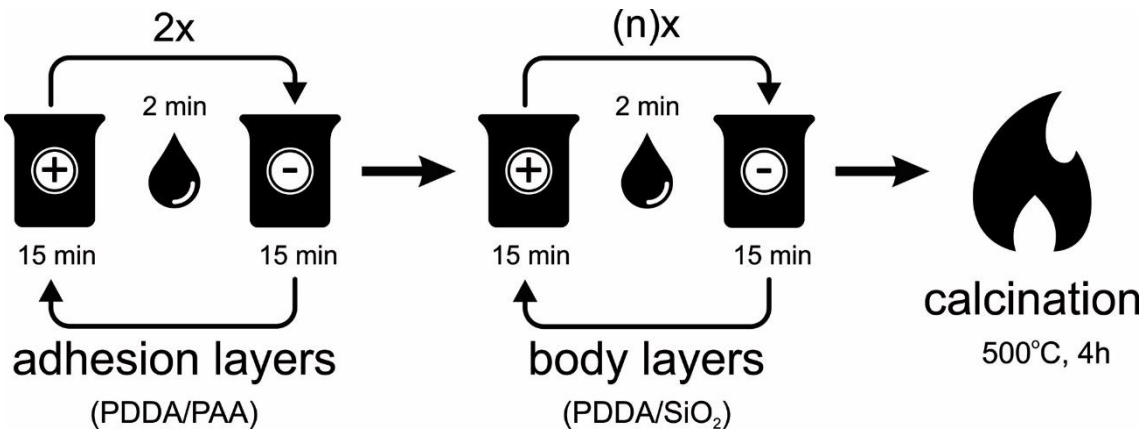

Figure 4.2 - Schematic illustration of the preparation protocol of the SiO_2-based coatings.

4.2.3 Surface modification

After the calcination step, uncoated glass slides (blank) and the selected compositions were chemically modified by being dipped in a 0.25 wt% trichlorododecylsilane solution in chloroform for 1h. Posteriorly to the hydrophobization process, specimens were rinsed with copious amount of chloroform and dried under N_2 flow in order to remove the non-reacted silane. For sake of simplicity, it is considered that all specimens are chemically identical after the hydrophobization step and identified by the notation “+silane”.

4.2.4 Characterization

The pH influence on the degree of ionization of PDDA and PAA was evaluated by attenuated total reflection-Fourier transform infrared spectroscopy (ATR-FTIR) performed in a Varian 640-IR equipment. Samples were prepared in the form of dried cast films onto glass slides. The pH values of polyelectrolyte aqueous solutions were adjusted with HCl and NaOH (0.2 M).

Stability of colloidal silica nanoparticles were evaluated by zeta potential measurements in a Dispersion Technology DT1200 equipment over a wide pH range.

Contact angle measurements were carried out at ambient temperature in a CAM 200 (KSV NIMA) equipment using 1μL (for hydrophilic samples) or 4μL (for hydrophobic samples) water droplets as indicators. WCA values were manually determined from the digital files captured by a CCD camera and, when possible, with the aid of the LB-ADSA plugin for ImageJ software [70]. Sliding angle (SA) values of hydrophobic surfaces were determined by the slow inclination of a tiltable plate until a 10μL water droplet starts to move.

Topographical information and root-mean-square roughness (RMS) values were determined by atomic force microscopy (AFM) using a NanoScope V (Bruker) equipment operating under contact mode at scan rate of 0.5 Hz. AFM data was processed using Gwyddion software.

Thickness and morphological properties of the coatings were analyzed from scanning electron microscopy (SEM) images obtained by a Magellan 400 L (FEI), a XL-30 FEG (Phillips) and/or a LEO 1530 FE SEM (Zeiss) equipment, depending on availability.

Transmittance measurements at normal incidence were performed using a Cary 50 Probe UV–visible spectrophotometer (Varian) operating in the entire visible light range.

5 RESULTS AND DISCUSSIONS

5.1 The suitable pH (around) 9

Once processing variables such as salt concentration [71], and temperature [72] play an important role in controlling molecular organization of strong polyelectrolytes, pH is a key factor in systems based on weak polyelectrolytes [73]. The pH influence on PDDA and PAA was analyzed by ATR-FTIR. Spectra of dry films casted from aqueous solutions prepared in a wide range of pH values are shown in Figure 5.1.

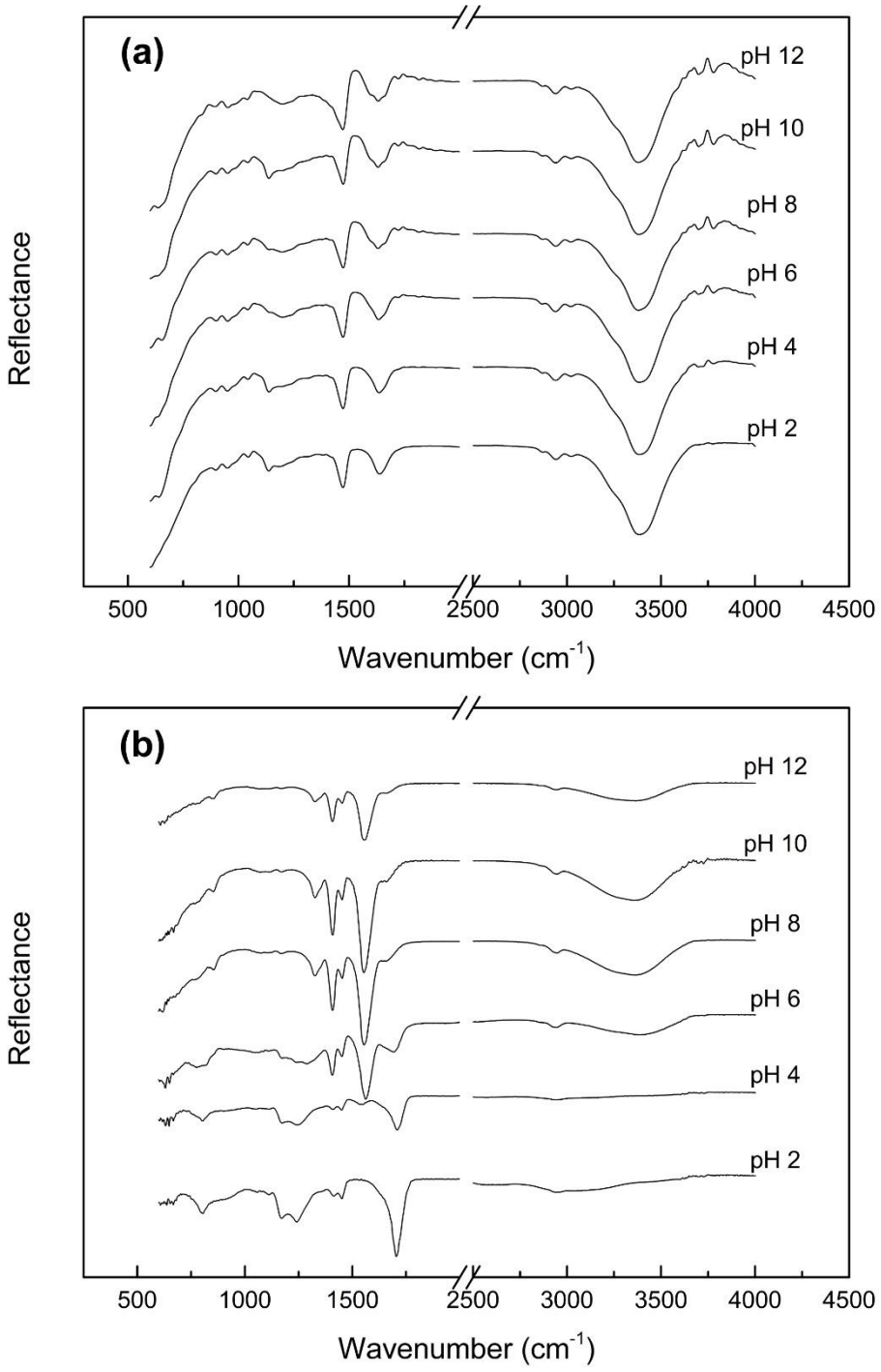

Figure 5.1 - ATR-FTIR spectra of (a) PDDA and (b) PAA films casted from aqueous solutions prepared with different pH values. Spectra are intentionally overlaid with arbitrary offset for clarity.

According to Figure 5.1a, PDDA seems not to be affected by the pH. Indeed, such behavior is more than expected since PDDA is a strong polycation

due to the quaternary ammonium group on its chemical structure; as a consequence, the degree of dissociation of ionic groups is nearly pH-independent over a wide pH range [74]. Concerning the PAA spectra (Figure 5.1b), two distinct peaks of the carboxylic acid functional groups are highlighted: one at υ = 1565 - 1542 cm^{-1} associated to the asymmetric stretching band of the ionized carboxylate (COO^-) group; and the other at υ ~ 1710 cm^{-1} attributed to the C=O stretching of the carboxylic acid (COOH) groups. In the acidic regime (pH 2), only the COOH acid peak was detected which indicates that essentially 100% of the functional groups of PAA exist in the non-ionized form. By increasing solution pH, the peak intensity of the COOH band decreased and the intensity of the COO^- band increased as the acid groups became ionized. Above pH 8, basically all COOH groups were transformed into the COO^- form, indicating a fully ionized state [73] and, as a consequence, providing enhanced adhesion to the substrate and to the subsequently deposited layers.

Despite the key role in the degree of ionization of weak polyelectrolytes, the pH should also be considered while working with colloidal nanoparticles. Probably, the most fundamental factors to create functional multilayer coatings based on nanoparticles are (i) control over z-direction placement and (ii) control over the aggregation level. The LbL process by itself provides the ability to place each layer in a fine-tuned manner whereas the manipulation of assembly conditions such as nanoparticle size, concentration and, especially, pH, provides the control over nanoparticle aggregation.

It is well-known that colloidal SiO_2 have a negative character due to the presence of silanol (-OH) groups on their surface; however, there is still no satisfactory method to determine the surface charge of small particles in aqueous suspensions. The common practice is to determine the electric potential at a location away from particle surface, in a region named slipping or shear plane. The potential measured at this plane is called zeta potential (ζ) and can be closely related to the suspension stability [75].

Since the surface charge of particles brought into contact with water are normally pH-sensitive [75,76], stability of 7nm, 22nm and 400nm SiO_2

suspensions was evaluated by zeta potential measurements over a wide range of pH values, as shown in Figure 5.2.

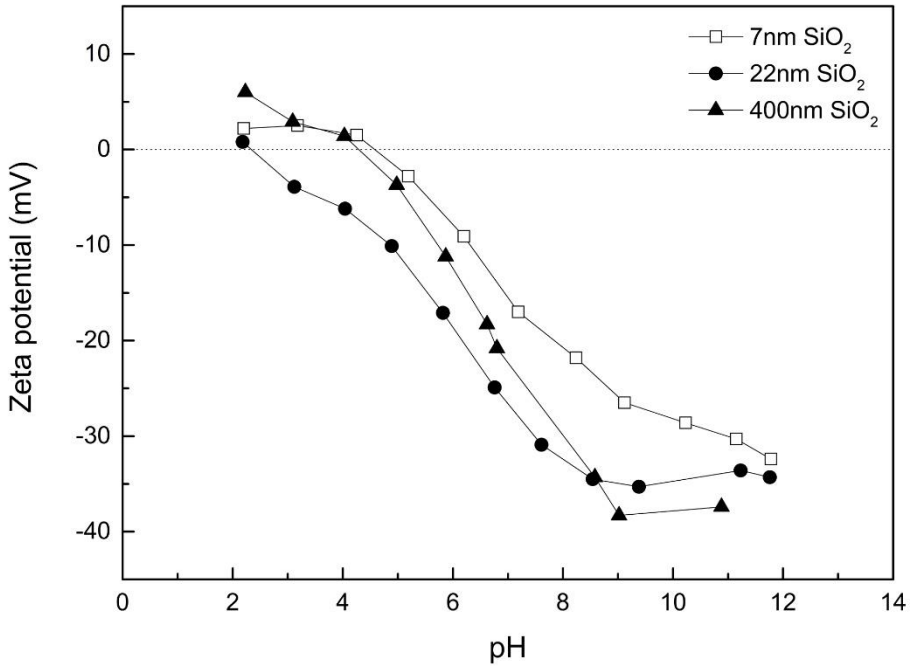

Figure 5.2 - Zeta potential measurements for 7nm, 22nm and 400nm SiO_2 aqueous suspensions over a wide range of pH values.

According to the Derjaguin, Landau, Verwey and Overbeek (DLVO) theory, highly stable colloidal systems are characterized by high |ʒ| values, whereas low |ʒ| indicate unstable systems. It is widely accepted that ʒ ± 30 mV are enough to promote stable water suspensions [77]. Intuitively one can infer that the presence of randomly shaped agglomerates in LbL dipping solutions might result in a deleterious effect over the control of the deposition process. From Figure 5.2, stability of all SiO_2 aqueous suspensions can be achieved at or above pH 8.

In summary, PDDA is a strong polycation, thus, pH-independent. On its turn, PAA is in the fully ionized state above pH 8 which is *precisely* the stability window of the three SiO_2 suspensions. So, taking advantage of such providential coincidence, pH ~ 9 was fixed for all dipping solutions and employed every single deposition step.

5.2 Nanoporous-driven superhydrophilicity

Before continuing, it is important to contextualize some topics. The project as a whole, but especially the experimental procedure, was designed to be *as simple as possible*. Thus, in a prior step, just the commercially available materials were employed in the preparation of the coatings. However, as soon as the structures become more sophisticated, large homemade 400nm SiO_2 were introduced to overcome technical limitations, widening the possibilities concerning structural manipulation and surface control. Naturally this subject will be recapitulated at the right moment, but, for now, it is important for the reader to follow the way towards the development of superhydrophilic SiO_2-based coatings. At this stage, the calcinated structures were not chemically modified with trichlorododecylsilane, taking advantage of the natural hydrophilic character of the small SiO_2 nanoparticles.

5.2.1 Topographic characterization

It is well-know that the wetting behavior of a surface is determined by both its chemistry and micro-nanotexture; as afore discussed, increasing the surface roughness of a given hydrophilic material might enhance its hydrophilicity. This phenomena is described by Wenzel's model [8] and is mathematically expressed by Equation (3.3)

In a first approach, concentration and particle size effect on wetting performance of SiO_2-based coatings prepared with 15 bilayers were investigated. Once wettability of a determined surface can be closely related to its roughness, topographic characterization were performed by atomic force microscopy (AFM). Root-mean-square (RMS) roughness values are reported in Table 5.1.

Table 5.1 - RMS roughness of uncoated glass and PDDA/SiO_2 coatings prepared with 15 bilayers

SiO_2 concentration (wt%)	RMS roughness (nm)		
	uncoated glass	PDDA/SiO_2 (7nm)	PDDA/SiO_2 (22nm)
0	~ 0	-	-
0.01	-	23	28
0.03	-	14	25
0.05	-	15	24
0.1	-	23	24

From Table 5.1, it is possible to observe that all PDDA/SiO_2 coatings exhibit rougher surface compared to uncoated glass. Enhanced roughness were attributed to the imperfect packing of SiO_2 nanoparticles. The AFM image of (PDDA/SiO_2 (22nm) 0.1%)$_{15}$ shown in Figure 5.3a reveals the structure typically observed from all specimens. Aggregated nanoparticles create hill-to-valley cavities illustrated by a cross-section thickness trace on Figure 5.3b.

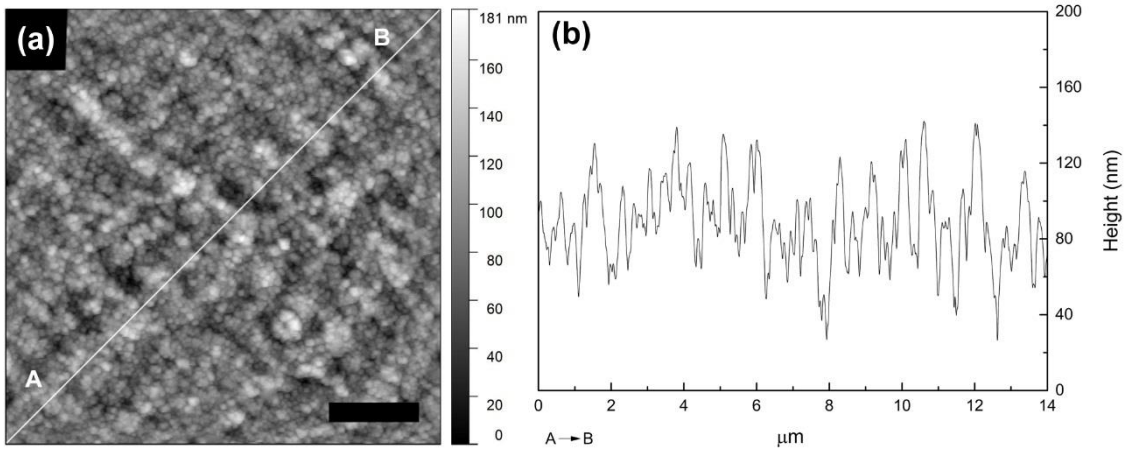

Figure 5.3 - AFM data of (PDDA/SiO_2 (22nm) 0.1%)$_{15}$ obtained from (a) height image; and (b) cross-section of the white line shown in (a). Scale bar: 2 µm.

Still from Table 5.1, neither particle size nor the concentration of SiO_2 suspensions seem to have a significant effect on surface roughness. At a first glance, this result was somehow unexpected since such parameters are normally related to nanoparticle aggregation, thus to the topography of multilayer films. Regarding Equation (3.3) and RMS roughness values obtained from AFM micrographs, it would be reasonable to infer that all coatings might exhibit a quite similar wetting behavior. Furthermore, one could also expect that hydrophilic character of SiO_2 allied to the rough nature of multilayer structures should provide ideal conditions for manifestation of superhydrophilicity.

5.2.2 Wettability of the coatings

In this way, the two differently sized colloidal silica nanoparticles were evaluated for their ability to promote a stable superhydrophilic state over different concentrations. Wettability of uncoated glass and PDDA/SiO_2 coatings as a function of time were evaluated by WCA measurements and the results are shown in Figure 5.4.

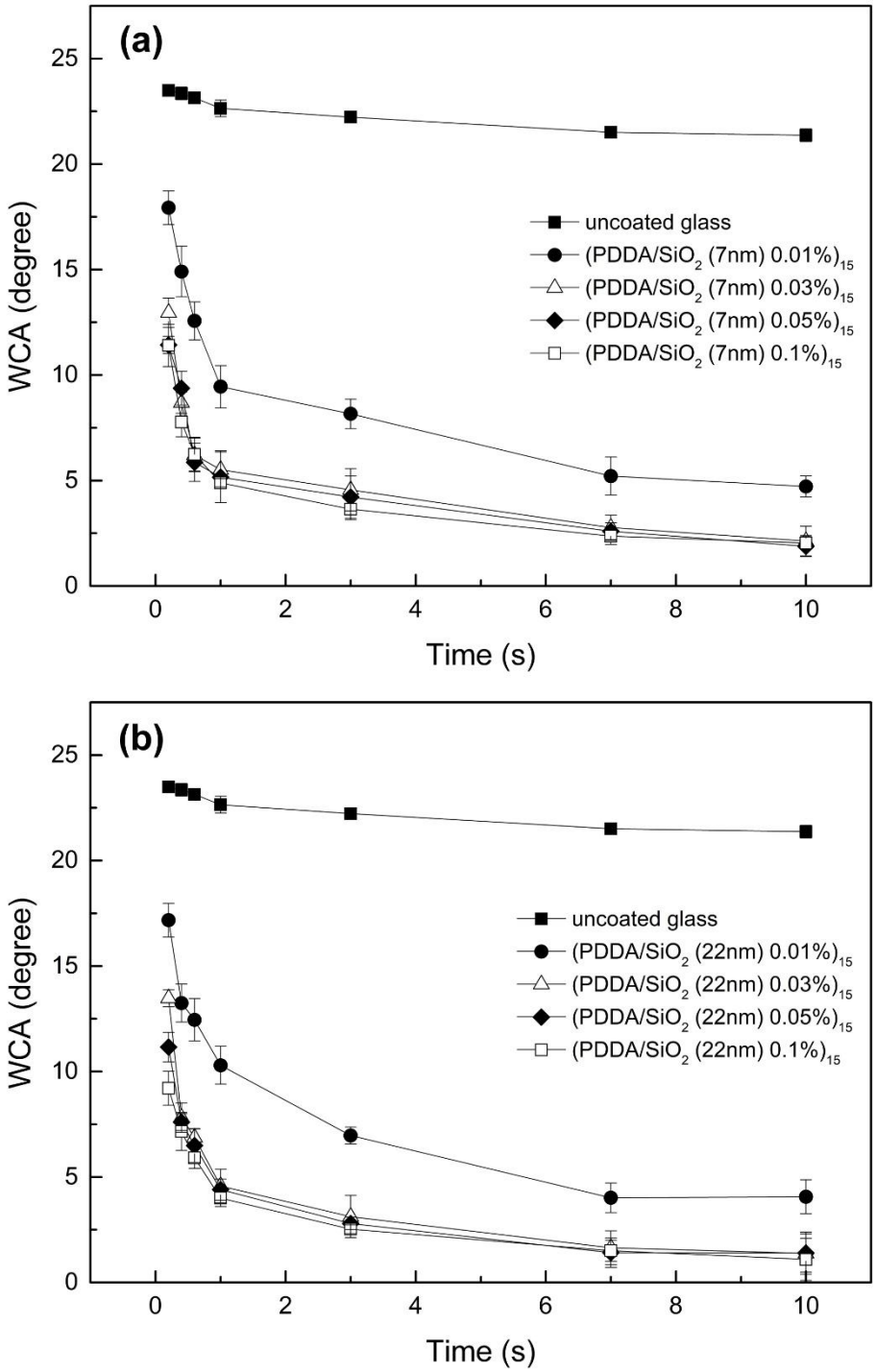

Figure 5.4 - WCA versus time of uncoated glass and PDDA/SiO_2 coatings prepared with (a) 7nm; and (b) 22nm SiO_2.

As aforementioned, superhydrophilic surfaces are normally described as on which WCA ≤ 5° within 0.5 s or less. According to Figure 5.4, except for (PDDA/SiO_2 (7nm) 0.01%)$_{15}$ and (PDDA/SiO_2 (22nm) 0.01%)$_{15}$, all specimens

exhibited virtually identical superhydrophilic behavior. In order to illustrate such wetting threshold, the WCA evolution over time of uncoated glass, $(PDDA/SiO_2$ (7nm) 0.01%$)_{15}$, $(PDDA/SiO_2$ (7nm) 0.03%$)_{15}$, $(PDDA/SiO_2$ (22nm) 0.01%$)_{15}$ and $(PDDA/SiO_2$ (22nm) 0.03%$)_{15}$ are shown in Figure 5.5.

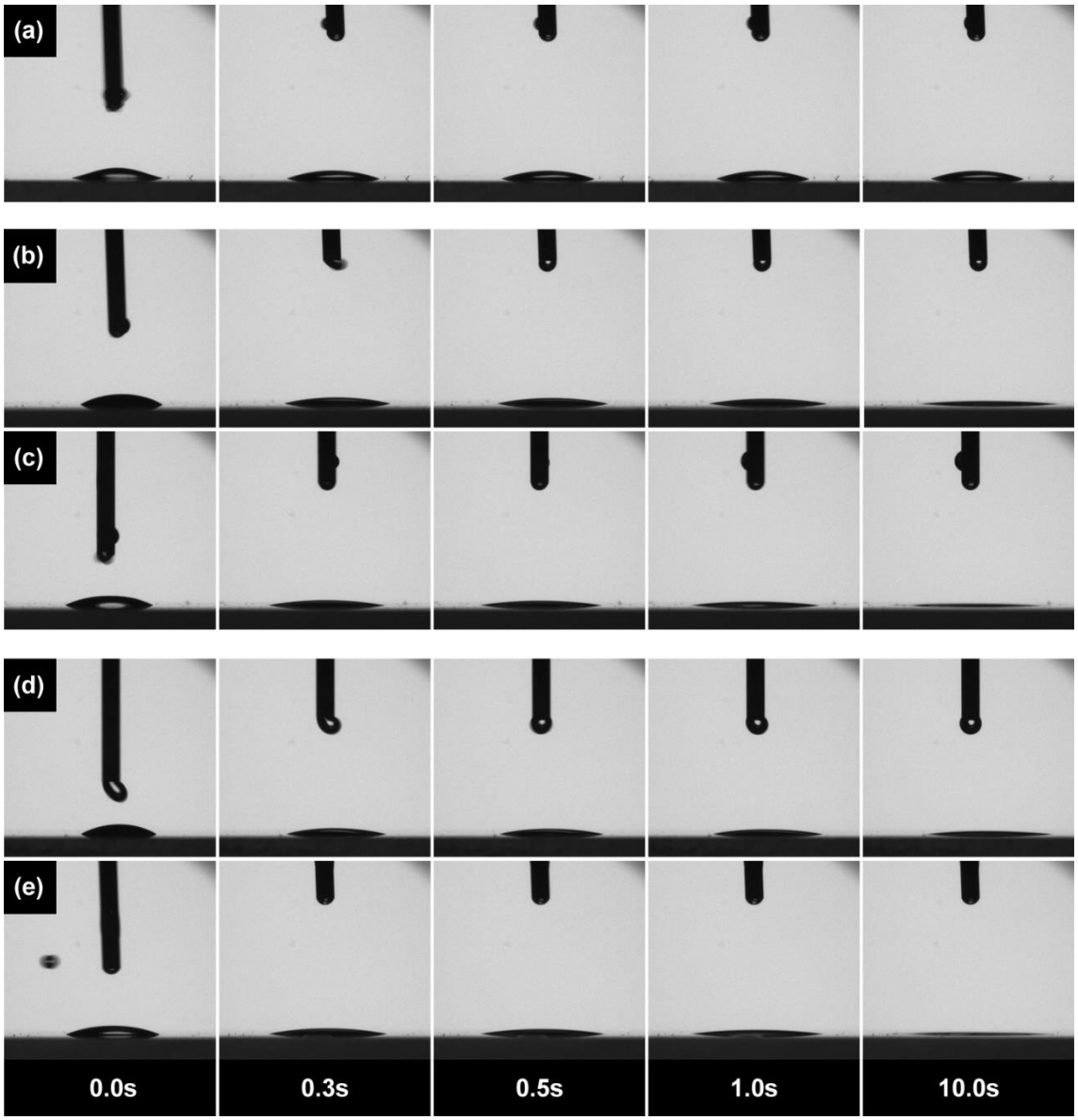

Figure 5.5 - WCA evolution over time for (a) uncoated glass; (b) $(PDDA/SiO_2$ (7nm) 0.01%$)_{15}$; (c) $(PDDA/SiO_2$ (7nm) 0.03%$)_{15}$; (d) $(PDDA/SiO_2$ (22nm) 0.01%$)_{15}$; and (e) $(PDDA/SiO_2$ (22nm) 0.03%$)_{15}$.

Considering the uniformity of superficial roughness values among all compositions, one can easily notice that both exceptions were not predicted by Wenzel's equation; therefore, adjusts on proposed model should be considered.

5.2.3 Structural properties

Bico et al. [78] examined theoretically the wettability of 2D–like porous surface. In this particular case, it was found that a *hemi-wicking* behavior (residing between droplet spreading and penetration) is possible. The critical contact angle (θ_c) below which a liquid will spontaneously infiltrate into the porous film is given by:

$$\cos\theta_c = \frac{1-\emptyset_s}{r-\emptyset_s} \tag{5.1}$$

where $\emptyset_s$ the solid fraction remaining dry during a wicking process; and r is the surface roughness factor. For a porous surface, r goes to infinity and the microstructure will be fully invaded by any liquid having an intrinsic CA ≤ 90º.

Cebeci et al. [79] suggested that surface roughness, although important, plays a secondary role in determining the wettability of porous SiO_2-based coatings. The primary mechanism was presumed to be the rapid water infiltration (nanowicking) in a 3D-wettable interconnected nanoporous network, described by Equation (5.1). According to the study, since superhydrophilic state was only observed at a critical film thickness (about 100 nm), it is suggested that the establishment of a *critical volume capacity* is the main responsible for enabling superhydrophilicity.

In order to verify whether such hypothesis applies to the current system, thickness of PDDA/SiO_2 coatings were measured by SEM images (Figure 5.6) and plotted against the concentration of SiO_2 in dipping suspensions, as shown in Figure 5.7.

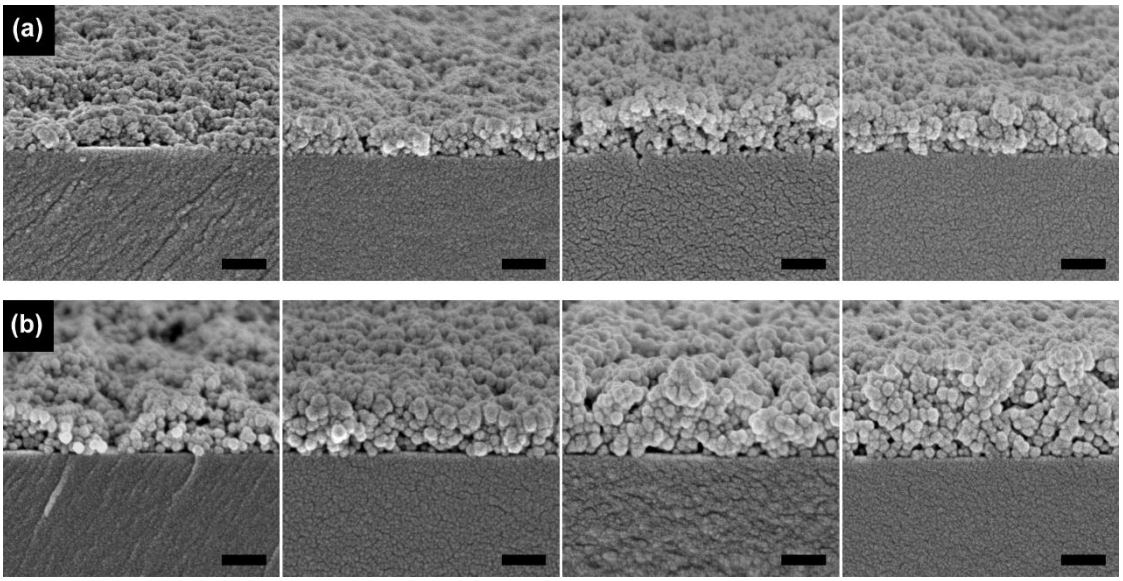

Figure 5.6 - *From left to right:* Cross-sectional SEM images of PDDA/SiO_2 coatings respectively prepared from 0.01 wt%; 0.03 wt%; 0.05 wt%; and 0.1 wt% dipping suspensions of (a) 7nm and (b) 22nm SiO_2. Micrographs were obtained from specimens tilted at 75° to the horizontal. Scale bar: 100nm.

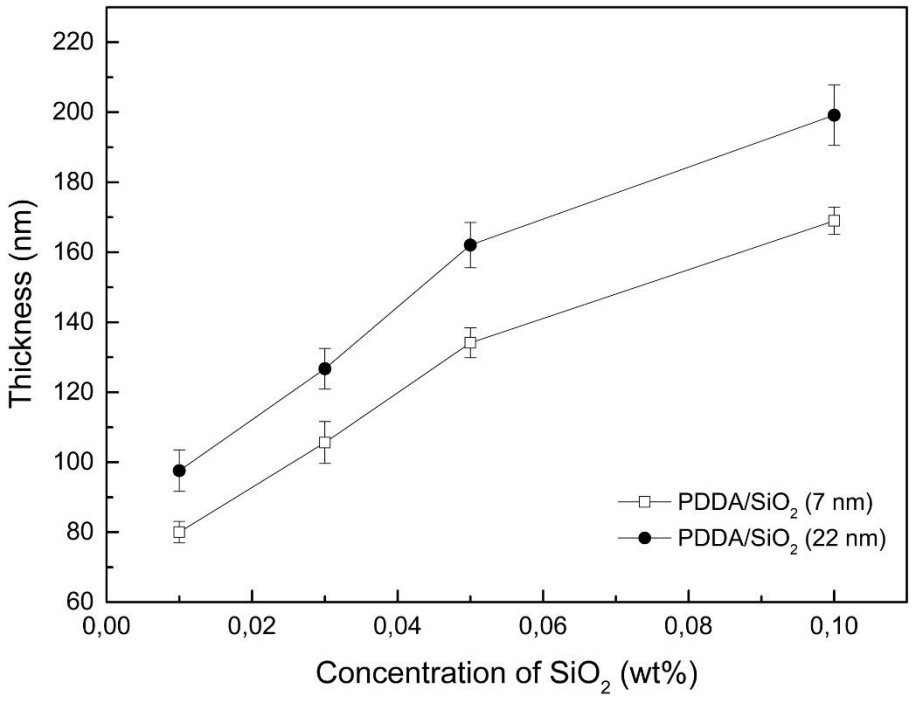

Figure 5.7 - Thickness of PDDA/SiO_2 coatings as a function of the concentration of SiO_2 dipping suspensions.

For both 7nm and 22nm SiO_2, increases in dipping suspension concentration are followed by corresponding increments in thickness of the coating. Briefly, at low SiO_2 concentration (until 0.05 wt%), growth of the films are basically linear; however, linearity deviation is observed at high nanoparticle concentration, giving room to an asymptotic-like behavior. The growth of SiO_2-based LbL coatings is ruled by a complex interaction of several parameters and have been explored in detail elsewhere [80–82].

Comparing Figure 5.4 and Figure 5.7 it is observed that, at least for the studied system, thickness and wettability might not be intimately related as expected. (PDDA/SiO_2 (22nm) 0.01%)$_{15}$ thickness is around 100 nm and did not manifested superhydrophilic behavior; concomitantly, (PDDA/SiO_2 (7nm) 0.03%)$_{15}$ exhibited almost the same thickness value, but, superhydrophilicity. Furthermore, even resulting in thicker structures, neither increases in concentration of SiO_2 suspension above 0.03 wt% nor in particle size were followed by a respective response of wetting behavior. In this way, it is not necessary to mention that the proposed hypothesis does not completely fit in the studied system and additional discussion is needed.

Some particularly interesting details can be observed in the SEM micrographs exhibited in Figure 5.8. The cross-sectional images reveal that the calcinated coatings are composed of loosely stacked SiO_2 nanoparticles, resulting in a nanoporous structure. It is also clear that both (PDDA/SiO_2 (7nm) 0.01%)$_{15}$ and (PDDA/SiO_2 (22nm) 0.01%)$_{15}$, respectively shown in Figure 5.8a and c, exhibit several defects along the surface. Such non-conformities, identified by the white arrows, seem to follow the same pattern and can be attributed to stacking failures during the deposition process. An attentive observer immediately infers that such defects probably are related to the shortage of nanoparticles during the assembly step.

Stacking defects are absent in all remaining compositions, suggesting the existence of a minimum SiO_2 concentration required for an effective deposition process. At the studied conditions, such hypothetical value might be laid between 0.01 wt% and 0.03 wt% of SiO_2. As shown in Figure 5.8b and d,

above such theoretical minimum concentration, homogeneous coatings are readily obtained.

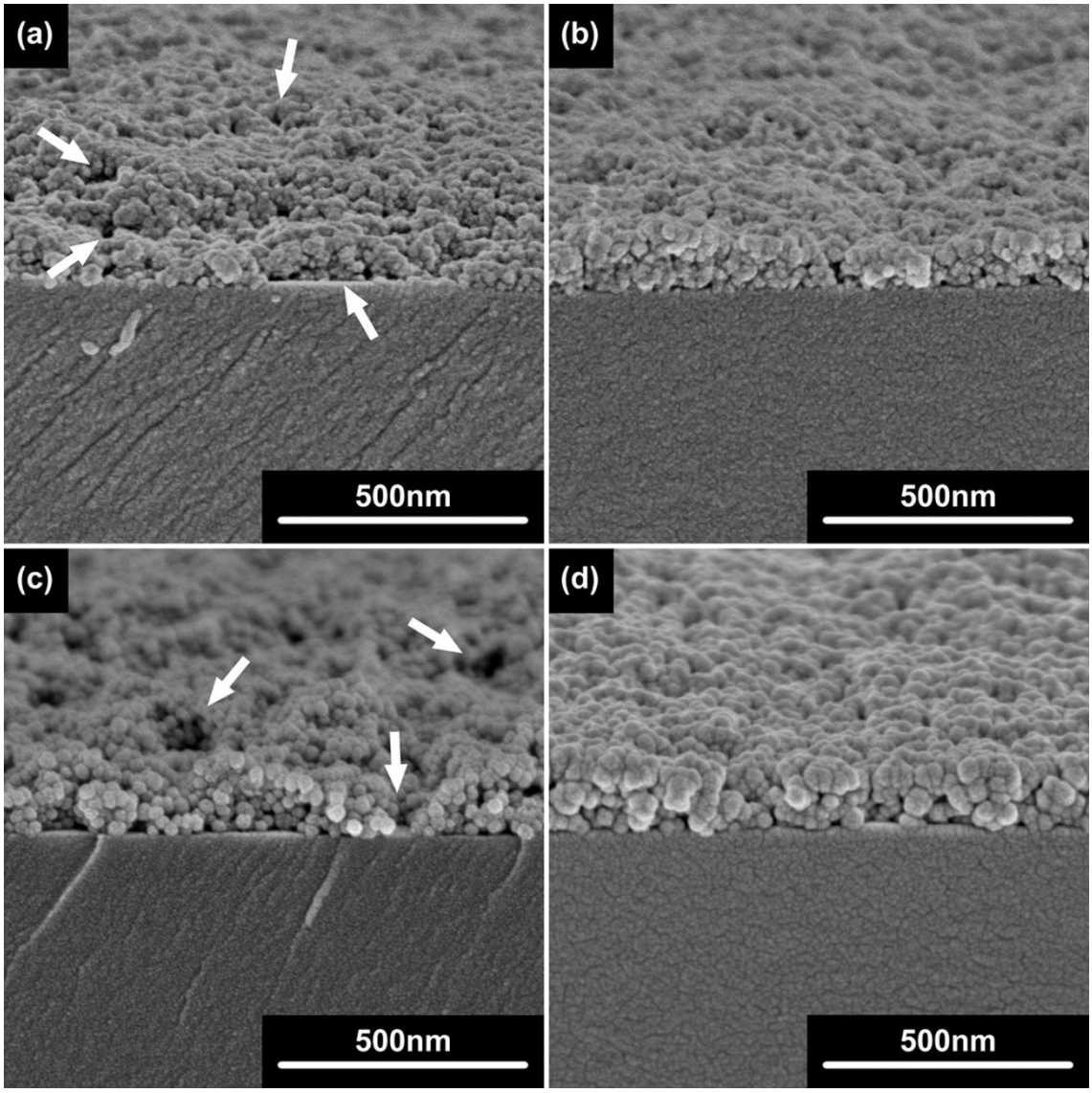

Figure 5.8 - Cross-sectional SEM images of (a) (PDDA/SiO_2 (7nm) 0.01%)$_{15}$; (b) (PDDA/SiO_2 (7nm) 0.03%)$_{15}$; (c) (PDDA/SiO_2 (22nm) 0.01%)$_{15}$ and (d) (PDDA/SiO_2 (22nm) 0.03%)$_{15}$. Micrographs were obtained from specimens tilted at 75° to the horizontal.

As previously mentioned, the rapid water infiltration into the porous structure is probably the primary mechanism governing superhydrophilicity of SiO_2-based coatings. Thus, here it is hypothesized that such non-homogeneities

on the 3D interconnected network hinder the formation of nanochannels and might be the responsible for the lower wetting performance of both (PDDA/ SiO_2 (7nm) 0.01%)$_{15}$ and (PDDA/SiO_2 (22nm) 0.01%)$_{15}$. The results also suggest that, contrary to previously reported [61,83], wetting performance is thickness-independent if a perfect nanoporous structure is stablished. In other words, if a uniform coating is obtained, superhydrophilic behavior is manifested. However, further increments in thickness might not be followed by a respective enhancement on the wetting performance.

5.2.4 Optical properties

Figure 5.9 shows the transmittance spectrum over the visible light range of uncoated glass and PDDA/SiO_2 coatings. The UV–vis analysis were performed in standard microscope glass slides covered just on one side.

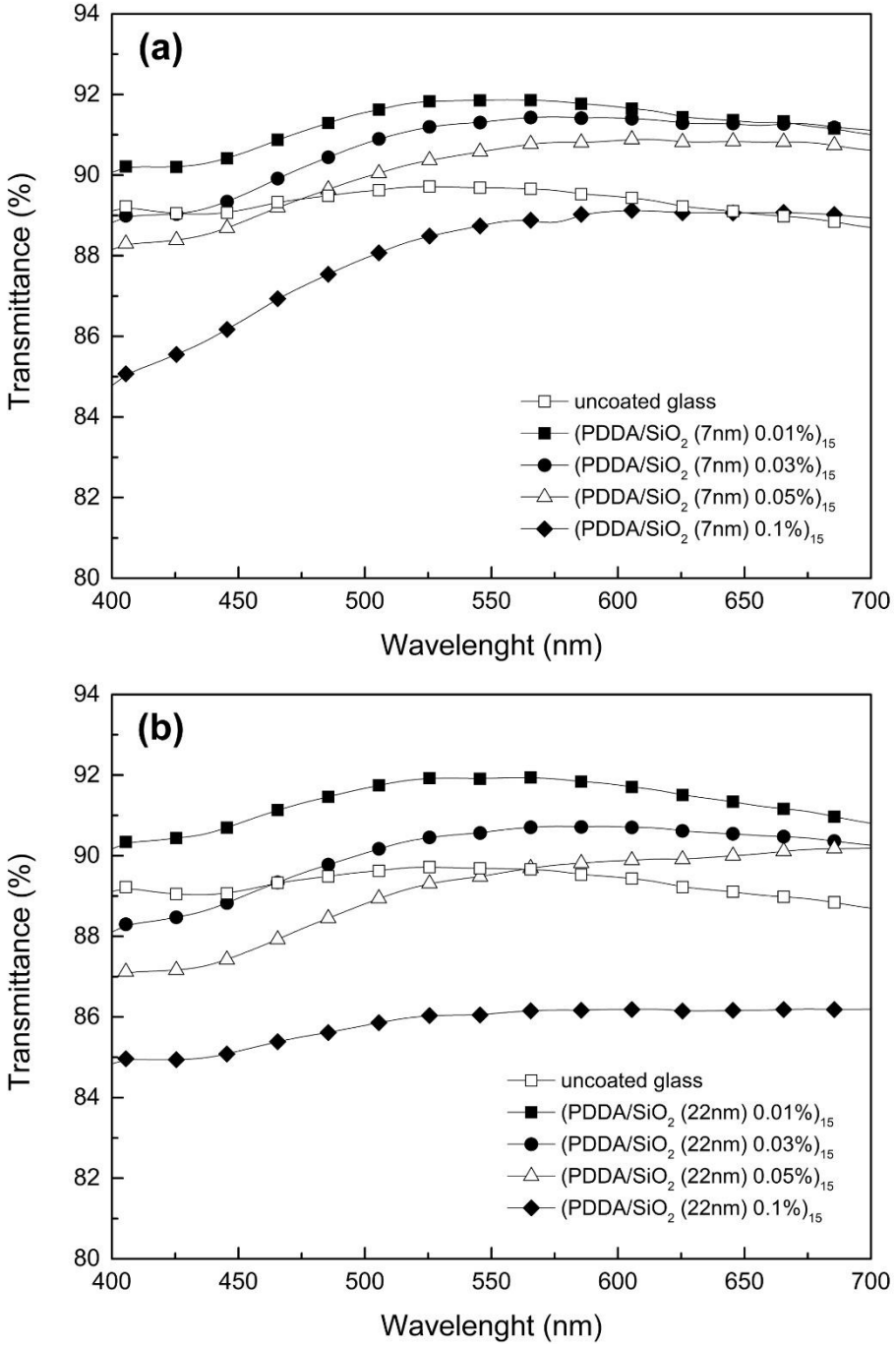

Figure 5.9 - Visible transmission spectra of uncoated glass and PDDA/SiO_2 coatings prepared with (a) 7nm and (b) 22nm SiO_2.

In general, all PDDA/SiO_2 coatings are highly transparent over the entire visible light spectrum. Compared to the uncoated glass, enhanced transmittance is observed for both (PDDA/SiO_2 (7nm) 0.01%)$_{15}$ and (PDDA/SiO_2 (22nm) 0.01%)$_{15}$ compositions, nevertheless increments in SiO_2 concentration are

invariably followed by respective reductions of transmitted light. Such behavior might be related to the competition between AR and light absorption effect. As previously reported [84], improvements of transmittance level can be attributed to the intrinsic antireflection (AR) feature of nanoporous coatings; in its turn, while thickness increases, light absorption effect becomes more relevant and transmittance is hampered.

Generally, when the refractive index (n_c) for an ideal homogeneous AR coating meets the condition expressed in Equation (5.2), reflection is suppressed at the wavelengths near the quarter-wavelength optical thickness:

$$n_c = (n_a n_s)^{1/2} \tag{5.2}$$

where n_a and n_s are, respectively, the refractive indices of the air and the substrate.

From Equation (5.2), for a glass substrate with n_s about 1.5, the maximum suppression of reflective losses occurs when an AR coating exhibit n_c = 1.22. Notwithstanding, natural materials with such low refractive indices are either rare or expensive to obtain in ultrathin film form. Fortunately, thickness-tuned nanoporous materials can be employed as suitable substitutes once the presence of nanoporosity can sharply reduce refractive index of the coating, therefore, satisfy the AR requirement [61].

5.2.5 Optimized properties balance

Superhydrophilic coatings can significantly reduce fogging effect due to the almost instantaneous spread of condensed water droplets in a thin sheet-like membrane; meanwhile, AR coatings can effectively enhance the substrates transmittance through the destructive interference between light reflected from the coating-substrate and the air-coating interfaces.

In a convenient way, the prepared SiO_2 multilayer nanoporous structures demonstrate the potential to integrate both antifogging and AR properties. For the studied system, (PDDA/SiO_2 (7nm) 0.03%)$_{15}$ seems to be the optimized

composition since, among the superhydrophilic coatings, it exhibited the highest transparency level over the entire visible light range. The antifogging effect and AR properties of (PDDA/SiO2 (7nm) 0.03%)$_{15}$ are respectively shown in Figure 5.10a-b.

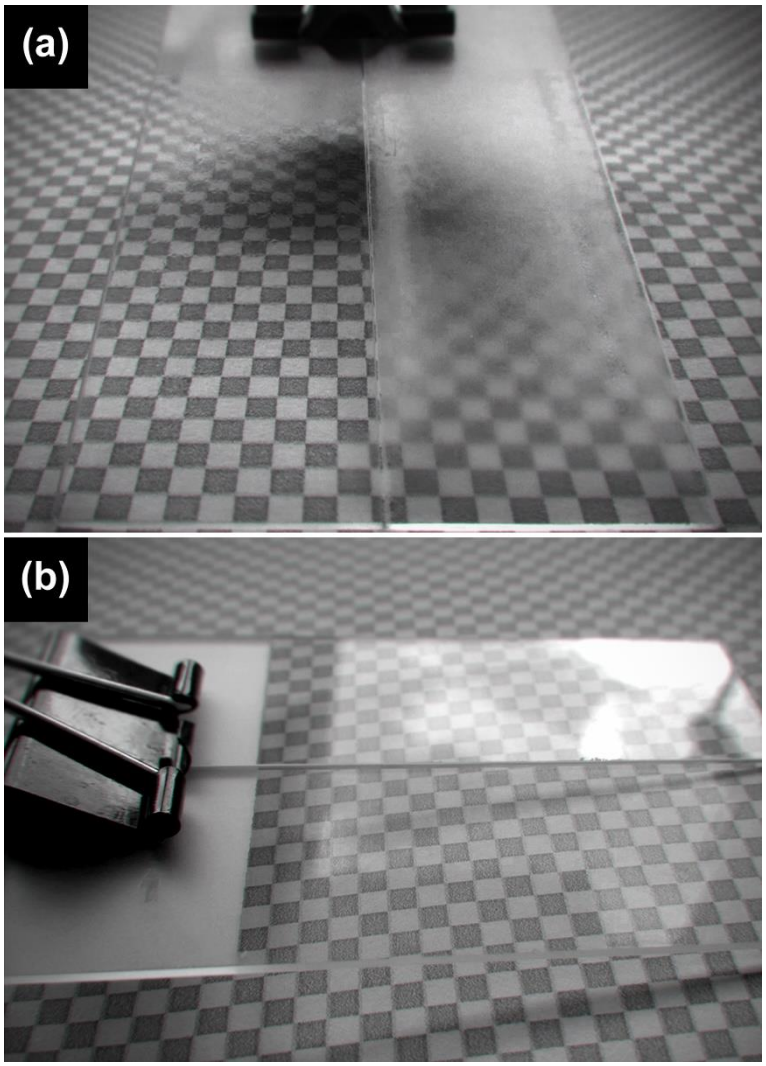

Figure 5.10 - (a) (PDDA/SiO_2 (7nm) 0.03%)$_{15}$ (left-hand side) and uncoated glass slide (right-hand side) taken from a refrigerator and immediately moved to humid air environment; (b) uncoated glass slide (topside) and (PDDA/SiO_2 (7nm) 0.03%)$_{15}$ (bottom side) exposed under natural light.

Figure 5.10a illustrates the antifogging behavior. Both glass slides were cooled in a refrigerator and immediately moved into humid air environment. The

glass slide coated with (PDDA/SiO_2 (7nm) 0.03%)$_{15}$ remained clear whereas the uncoated glass slide fogged immediately. From Figure 5.10b, the AR property of (PDDA/SiO_2 (7nm) 0.03%)$_{15}$ coating is nicely revealed when exposed to natural light.

5.3 Hierarchical roughness-driven superhydrophobicity

Transparent AR superhydrophilic nano- porous/rough coatings were prepared via LbL assembly of PDDA/SiO_2 and, by tuning the concentration of SiO_2 dipping suspension, uniform structures could be obtained. Nevertheless, as almost a science's postulate, for every answer - new questions are always arisen. At this point, a possible question would be if superhydrophobicity can be induced in the studied system by a suitable chemical modification.

From the earlier discussion, 0.03 wt% suspensions of both 7nm and 22nm SiO_2 is enough to ensure a highly homogeneous structure after 15 assembly cycles. It is also possible to infer that larger nanospheres potentially provide a superior surface roughness due to the difficulty in the packing process. Thus, despite the slightly better optical properties of 7nm SiO_2-based coatings, (PDDA/SiO_2 (22nm) 0.03%)$_{15}$ was selected as the starting point for the next step.

Once SiO_2 concentration did not show itself as a suitable alternative to control the surface roughness, a different approach based on the number of deposited bilayers is proposed. In this context, (PDDA/SiO_2 (22nm) 0.03%)$_n$ were prepared via LbL assembly and chemically modified with trichlorododecylsilane.

5.3.1 Random roughened surfaces

The AFM micrographs exhibited in Figure 5.11 reveals the evolution of the topography of (PDDA/SiO_2 (22nm) 0.03%)$_n$+silane coatings as a function of the number of n assembly cycles.

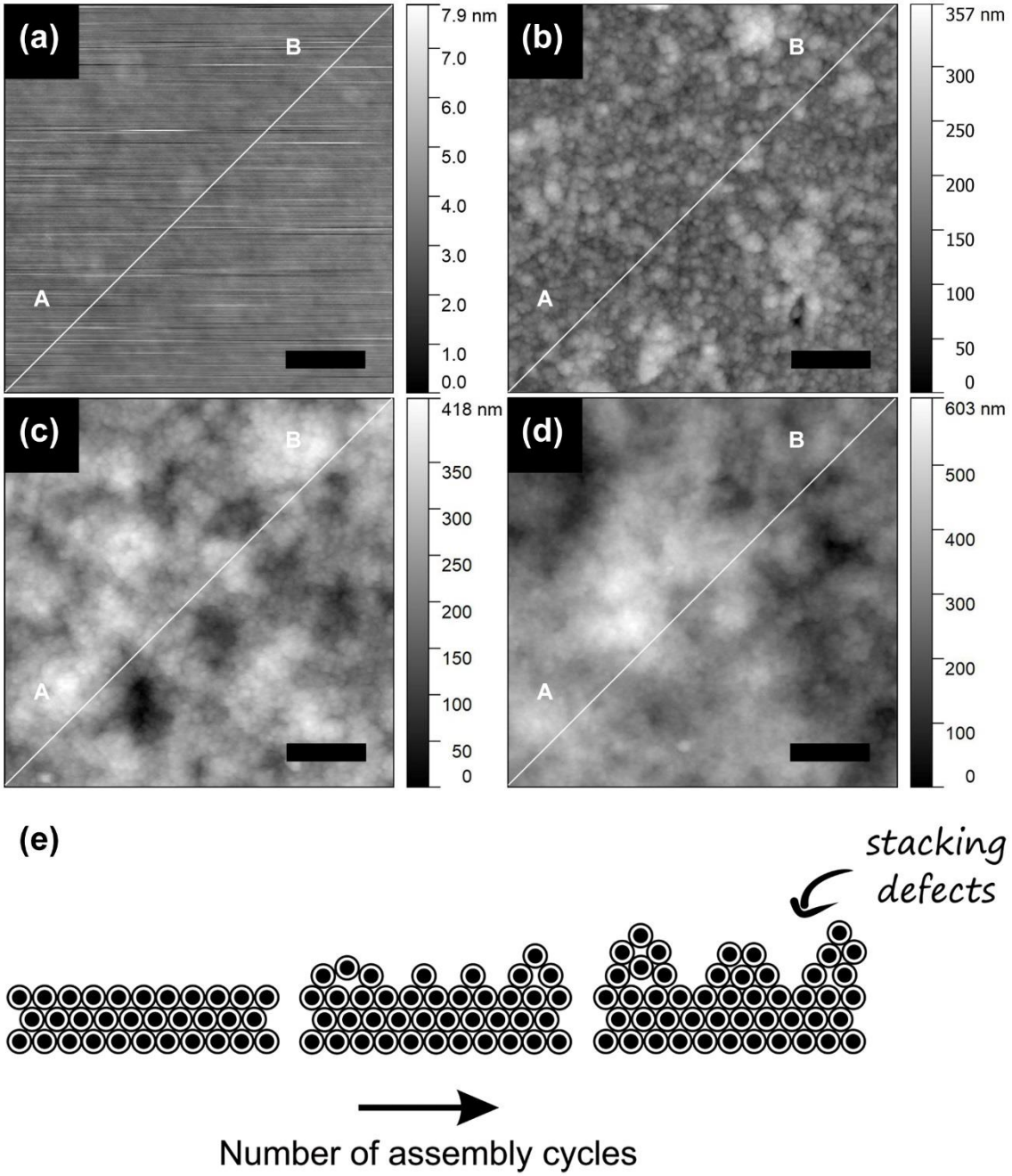

Figure 5.11 - AFM data of $(PDDA/SiO_2$ (22nm) $0.03\%)_n$+silane where n is equal to (a) 0 (uncoated glass); (b) 15; (c) 30; (d) 45; and (e) schematic illustration of topographic evolution as a function of the number of assembly cycles. Scale bar: 2µm

From Figure 5.11a-d, it is possible to evolve from slightly nanorough surfaces into hierarchical hill-and-valley structures just by increasing the number of deposited PDDA/SiO2 (22nm) bilayers. This behavior might be related to the

aggregation and/or non-uniform adsorption of the silica nanoparticles, responsible for stacking defects and the formation of a random roughened topography. The height of asperities also seems to be related to the number of deposited bilayers, as schematically shown in Figure 5.11e. The cross-section of the white lines traced in Figure 5.11a-d is shown in Figure 5.12.

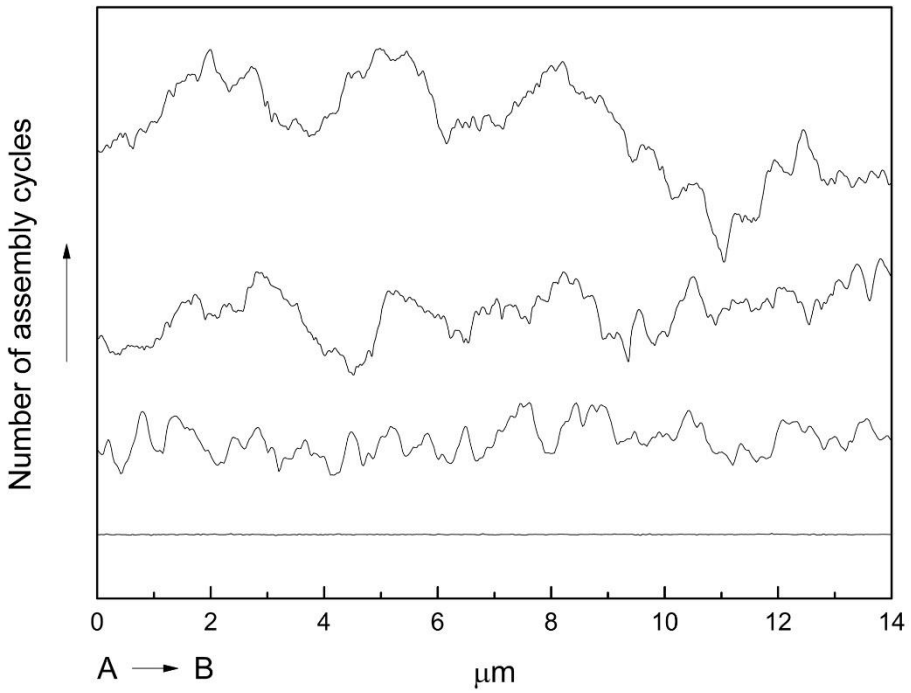

Figure 5.12 - *From the bottom to the top*: Cross-sections of the white lines traced in Figure 5.11a-d of $(PDDA/SiO_2$ (22nm) 0.03%$)_n$+silane where n is respectively equal to 0 (uncoated glass); 15; 30 and 45. The surface profiles are intentionally overlaid with arbitrary offset for clarity

Once lotus effect is normally attributed to the synergy between roughness and low surface energy, it would be reasonable to expect an increase in the hydrophobicity with the increase of the number of deposited bilayers. RMS roughness, WCA and SA and values of the chemically modified uncoated glass (blank) and $(PDDA/SiO_2$ (22nm) 0.03%$)_n$+silane coatings are shown in Table 5.2.

Table 5.2 - RMS roughness, WCA and SA values of uncoated glass and $(PDDA/SiO_2$ (22nm) 0.03%$)_n$+silane coatings

Composition	RMS roughness (nm)	WCA (º)	SA (º)
uncoated glass	~ 0	103 ± 3	> 30
$(PDDA/SiO_2$ (22nm) 0.03%$)_{15}$+silane	36	128 ± 2	> 30
$(PDDA/SiO_2$ (22nm) 0.03%$)_{30}$+silane	60	132 ± 3	> 30
$(PDDA/SiO_2$ (22nm) 0.03%$)_{45}$+silane	90	134 ± 6	> 30

According to Table 5.2, all surfaces are sticky (high SA values), then Wenzel regime [8] should be considered. From the Equation (3.3), compared to the uncoated glass, all SiO_2-based coatings will invariably exhibit improved hydrophobicity once the actual surface of the particulate films will always be higher than the its respective geometric surface, here, represented by the smooth glass slides.

However, especially for nanoscale structures, measuring the actual surface is not a trivial task; therefore, RMS roughness has extensively been employed as an indicator of roughness factor r. As a result, correlations between wettability of solid surfaces and RMS roughness were proposed [23,63,85–87]. In this study, the wettability of $(PDDA/SiO_2$ (22nm) 0.03%$)_n$+silane was not affected neither by the RMS roughness nor by the different surface morphologies obtained through the number of assembly cycles (Figure 5.13).

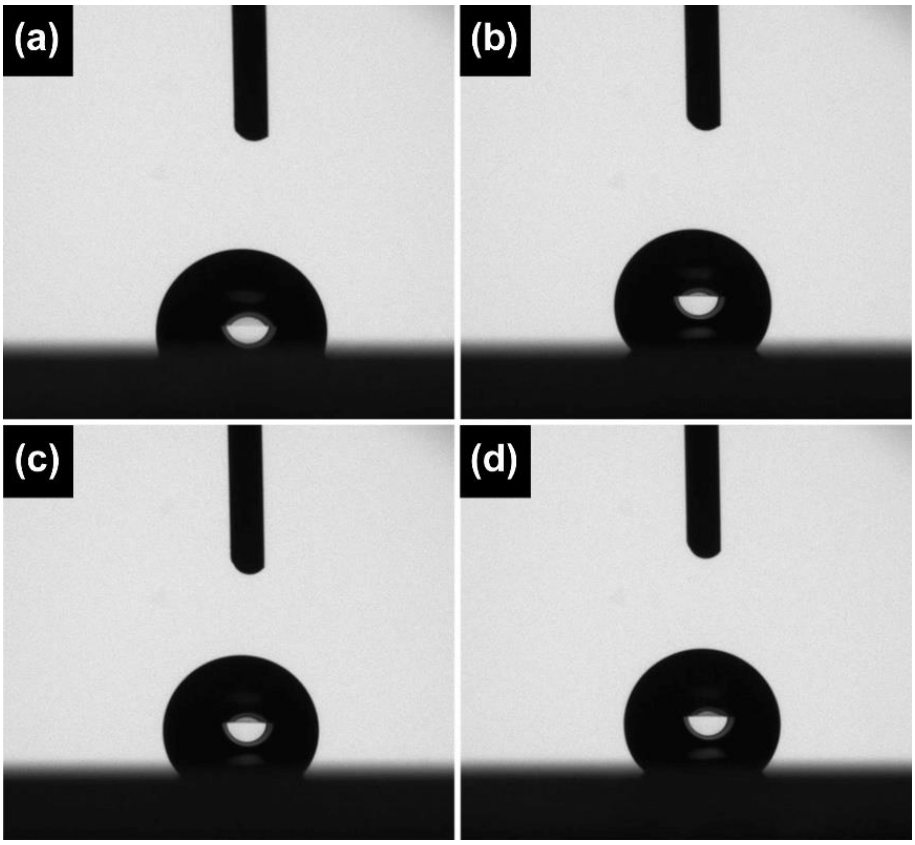

Figure 5.13 - Wettability of (a) uncoated glass; (b) $(PDDA/SiO_2\,(22nm)\ 0.03\%)_{15}$; (c) $(PDDA/SiO_2\ (22nm)\ 0.03\%)_{30}$ and; (d) $(PDDA/SiO_2\ (22nm)\ 0.03\%)_{45}$

In 1949, as a *communication to the editor* [88], Wenzel clarified that the roughness responsible for modifying wetting characteristics is defined as the ratio of the area of the actual surface to that of a smooth surface having the same geometric shape and dimensions. In this way, roughness factor r cannot be determined by measurement of surface profiles and has no relation to the root mean square (RMS) of deviations from mean elevation [89–91].

5.3.2 Wettability of random roughened surfaces

The absence of a direct correspondence among RMS roughness and r can be rationalized if one consider that the *actual surface area* A of a rough

structure strongly depends on the local surface slopes (∇h), as mathematically defined by [92]:

$$A = \iint \sqrt{1 + \nabla h^2}\ dx\ dy \tag{5.3}$$

where $\nabla h^2 = (\partial h/\partial x)^2 + (\partial h/\partial y)^2$. In other words, A is a function of the hybrid parameter ∇h which, contrary to the RMS roughness, takes into account not only the heights of peaks and valleys but also the lateral features of the studied surface [93,94].

It has been recurrently proposed that a reliable correlation between the WCA and r can obtained from AFM micrographs [95–99]. In order to validate such procedure, a routine employing the Lagrange interpolation polynomial method was written in MATLAB [100] *(see Appendix A)* and rigorous calculations of surface areas A from AFM data were performed. The experimental roughness factor r_{exp} calculated by dividing each A value by their respective projected AFM areas are presented in Table 5.3.

Table 5.3 - Experimental roughness factor r_{exp} values of uncoated glass and (PDDA/SiO_2 (22nm) 0.03%)$_n$+silane coatings

Composition	Experimental roughness factor (r_{exp})
uncoated glass	~ 1
(PDDA/SiO_2 (22nm) 0.03%)$_{15}$+silane	1.05
(PDDA/SiO_2 (22nm) 0.03%)$_{30}$+silane	1.02
(PDDA/SiO_2 (22nm) 0.03%)$_{45}$+silane	1.03

Table 5.3 evidences that, unlike RMS roughness, r_{exp} are virtually constant and close to the unity for all compositions; thus, WCA values of the particulate coatings are 25 - 30° larger than the predicted by Equation (3.3). Such divergence might be related to the limited resolution of the AFM equipment,

supposed to be sensible to the microscale hill-and-valley topography but not to the nanoroughness arising from the 22nm SiO_2 nanoparticles.

If true, the microscale roughness did not affect the r_{exp} values and consequently has a negligible contribution on wettability of (PDDA/SiO_2 (22nm) 0.03%)$_n$+silane coatings. Therefore, wettability is being exclusively ruled by the local nanoroughness, responsible for maintaining the WCA values of the coatings close to each other and always larger than the uncoated glass. Indeed, it has been shown that close-packed monolayer of small nanospheres results in an apparent contact angle of about 120° for $\theta_e \sim 105°$ [101,102].

5.3.3 The unlikely transition from Wenzel to Cassie-Baxter state

It is well-known that if significant amount of air is entrapped within the multiscale asperities, large WCA values are expected and mathematically described by Cassie-Baxter model [9].

For the studied system, even in hill-and-valley hierarchical structures such as (PDDA/SiO_2 (22nm) 0.03%)$_{45}$+silane, Wenzel state was exclusively manifested. So, considering the topographical evolution of (PDDA/SiO_2 (22nm) 0.03%)$_n$+silane coatings, the natural question is why the transition from Wenzel to Cassie-Baxter state was not observed. In other words, theoretically speaking, would it be possible to induce a specific wetting regime just by controlling the number of deposited PDDA/SiO_2 (22nm) bilayers?

One possible approach for elucidating this problem might be laid on stability criteria for a solid-liquid-gas interphase. Figure 5.14 illustrates air entrapped between two asperities of height H separated by a distance D.

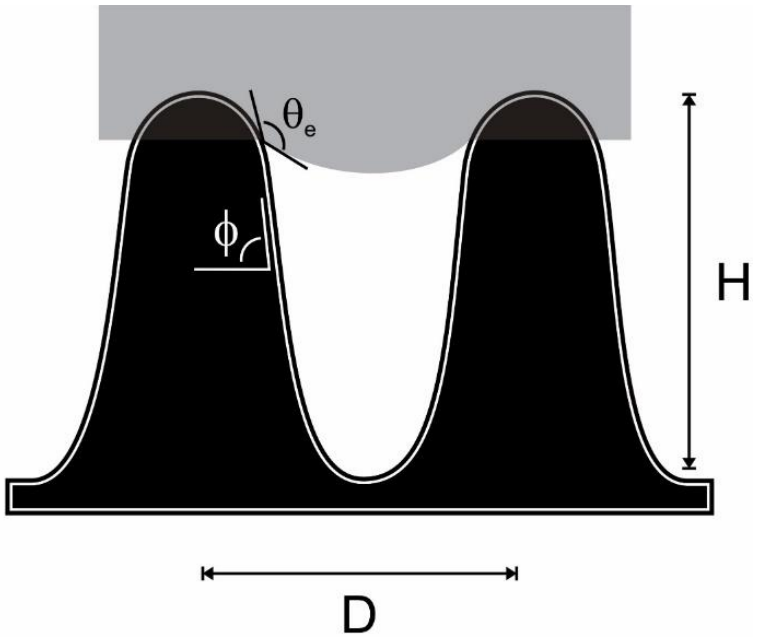

Figure 5.14 - Schematic illustration of a solid-liquid-gas interphase with air entrapped between two asperities;

It has been shown that such complex interphase becomes stable if Inequation (5.4) is satisfied; if not, the liquid-solid contact line will spread to satisfy Young's law [103] and a fully wetted Wenzel state takes place [104–109].

$$\Phi > (180 - \theta_e)^{\circ} \tag{5.4}$$

where Φ is the local inclination angle; and θ_e is the local contact angle between the liquid and the solid surface.

Since the tangent of Φ is precisely given by the local surface slope, the distribution of Φ values for of (PDDA/SiO_2 (22nm) 0.03%)$_n$+silane coatings were experimentally determined by applying the ∇h parameter from Equation (5.3) on AFM data. The results are shown in Figure 5.15.

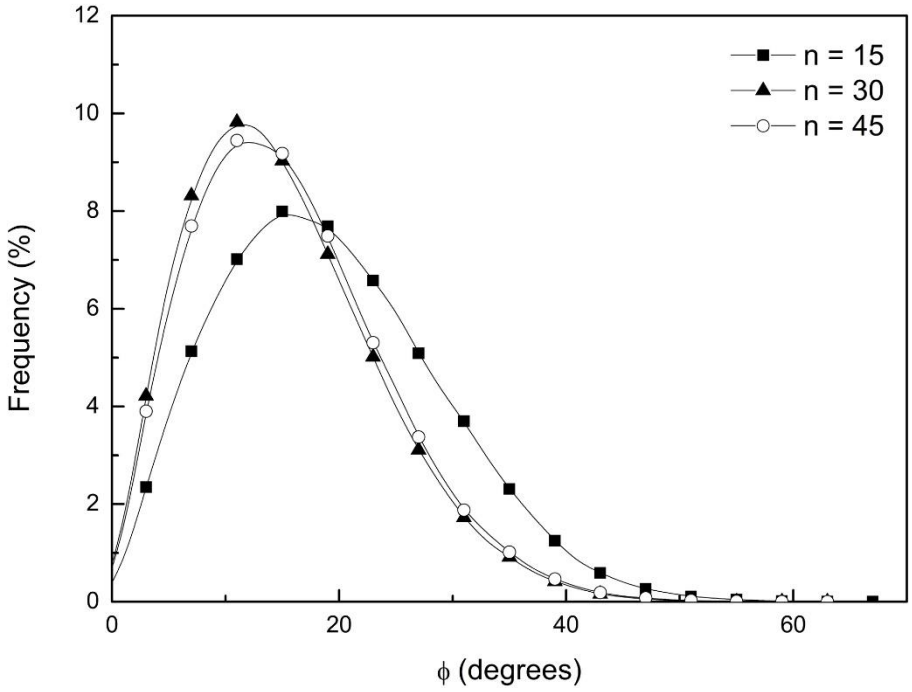

Figure 5.15 - Frequency distribution of Φ values for (PDDA/SiO_2 (22nm) 0.03%)$_n$+silane coatings.

For the studied system, θ_e should be obtained from a close-packed monolayer of 22nm SiO_2. However, (PDDA/SiO_2 (22nm) 0.03%)$_{15}$+silane shows itself as a reasonable candidate for such estimation since it is essentially plane. Therefore $\theta_e \sim 128°$ and, according to Inequation (5.4), stabilization of the solid-liquid-air interphase would take place above a critical value of $\Phi_{crit} > 52°$. Well, Figure 5.15 reveals that no fraction of asperities satisfies such criteria for any composition and, as mathematically predicted, a fully wetted Wenzel state was exclusively manifested in the (PDDA/SiO_2 (22nm) 0.03%)$_n$+silane system.

As observed from Figure 5.15, even though the RMS height increases strongly, Φ values curiously do not show a significant increasing as more bilayers are deposited on surface. For random roughened surfaces, the *average slope* is the ratio of the average height to the average width of the asperities. While the average height is proportional to RMS height, the average width can be estimated by extrapolating the surface roughness to a superimposition of sinusoidal components. In this case, topography can be mathematically modeled by the autocorrelation function $ACF(\tau)$, which gives the relation between two

consecutive height points $h(x)$ and $h(x+\tau)$, separated by a distance (τ) [110,111]:

$$ACF(\tau) = \lim_{L\to\infty} \frac{1}{\sigma^2 L} \int_0^L h(x)\, h(x+\tau) dx \quad (5.5)$$

where σ is the RMS height and L is the sample length. Fortunately, for several cases, $ACF(\tau)$ can be expressed by an exponential function:

$$ACF(\tau) = \sigma^2 \exp\left(-\frac{\tau}{\beta}\right) \quad (5.6)$$

where β is the correlation length.

In a tangible way, the correlation length (β) is interpreted as an average of the widths of the surface asperities. Thus, by determining σ and β, one can easily describe the key parameters of a given random roughened surface where the ratio σ/β is proportional to its average slope [111–113]. The calculated σ and β parameters of (PDDA/SiO_2 (22nm) 0.03%)$_n$+silane coatings are expressed in Table 5.4.

Table 5.4 - σ and β parameters of (PDDA/SiO_2 (22nm) 0.03%)$_n$+silane coatings

Composition	RMS height (σ)	Correlation length (β)
(PDDA/SiO_2 (22nm) 0.03%)$_{15}$+silane	36	330
(PDDA/SiO_2 (22nm) 0.03%)$_{30}$+silane	60	600
(PDDA/SiO_2 (22nm) 0.03%)$_{45}$+silane	89	1200

In this way, σ/β values are 0.11, 0.10 and 0.07 respectively for n = 15, 30 and 45. By a simple linear regression, one can conclude that there is no significant dependency (p-value = 0.18) between the σ/β and n. Thus, it is not possible to assert that the average slope of (PDDA/SiO_2 (22nm) 0.03%)$_n$ is affected by the number of deposited bilayers.

Indeed, at least concerning the effect on wettability, σ/β variation seems to be negligible. In other words, the continuous deposition of PDDA/SiO_2 (22nm) bilayers increased the average height of the surface asperities; however, it simultaneously increased the average width at a similar rate. As a result, the average slope remained virtually constant and no changes in the WCA values were observed.

5.3.4 Wettability of non-close packed raspberry-like surfaces

It was demonstrated that increasing the number of deposited PDDA/SiO_2 (22nm) bilayers is not a suitable alternative to create superhydrophobic coatings. As an intrinsic feature of the LbL assembly of the studied system, the average slope of coatings based on small SiO_2 nanoparticles seems to be independent of the number of assembling cycles, resulting in a constant and low WCA value.

In order to achieve a different type of hierarchical topography, a creative but well-known approach was employed [114–117]. As schematically shown in Figure 5.16a, a particular structure can be obtained through the deposition of small particles over first deposited large particles. Such structure is commonly known as raspberry-like morphology and was prepared through the deposition of (PDDA/SiO_2 (400nm) 0.03%)$_{12}$, followed by the deposition of (PDDA/SiO_2 (22nm) 0.03%)$_3$. This fine-tuned composition is named as (PDDA/SiO_2 (400nm+22nm) 0.03%)$_{12+3}$+silane.

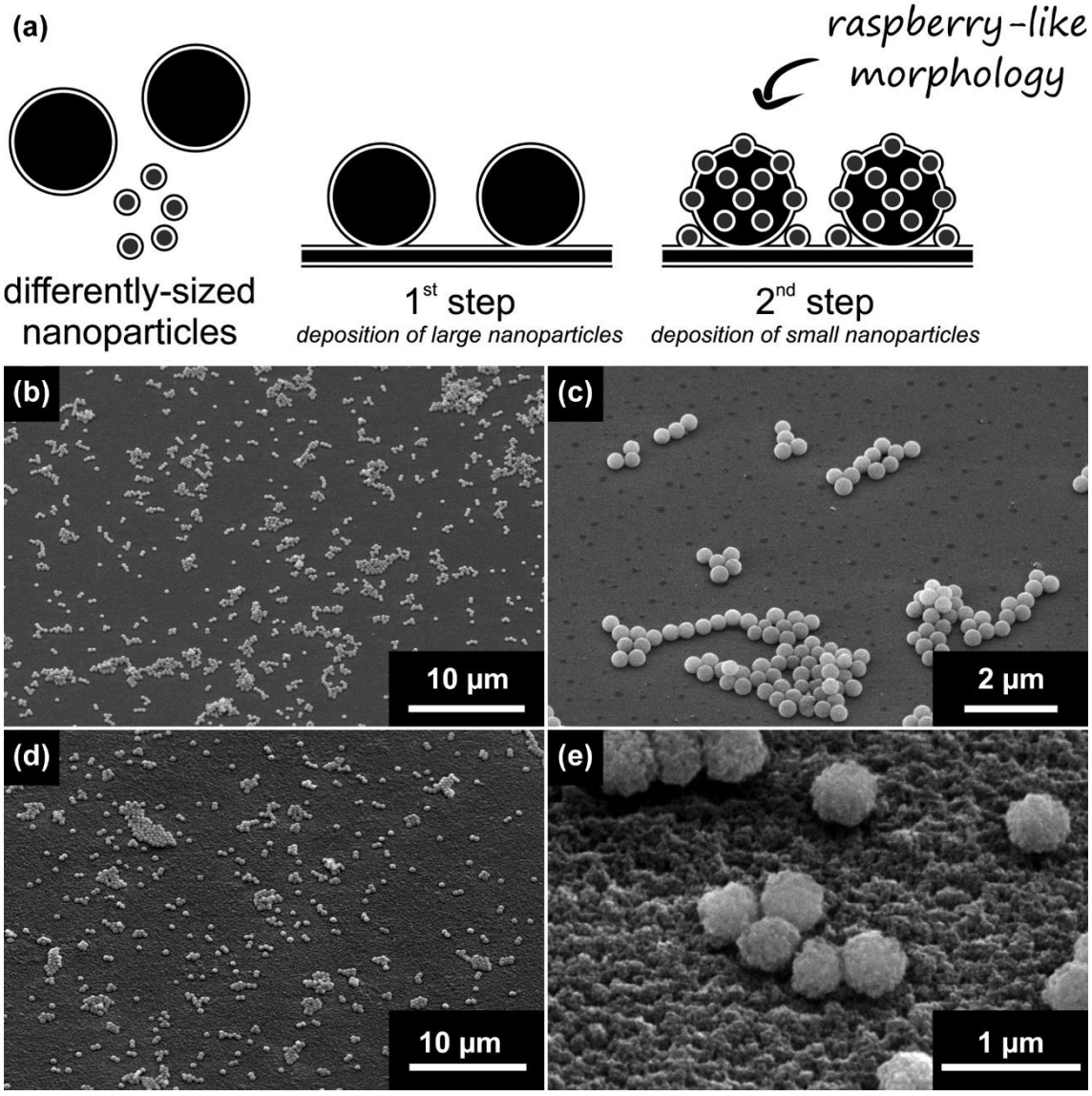

Figure 5.16 - (a) Schematic illustration of the two-step deposition process employed in the preparation of coatings with raspberry-like morphology; SEM images with different magnifications of (b - c) (PDDA/SiO_2 (400nm) 0.03%)12+silane; and (d - e) (PDDA/SiO_2 (400nm+22nm) 0.03%)12+3+silane. Micrographs were obtained from the top of specimens tilted at 45° to the horizontal.

The resulting coatings, we must admit, were slightly different from the expected. From Figure 5.16b and c, the assembly process of the large SiO_2 nanoparticles was very inefficient. Rather than a thick close-packed structure, it is observed a barely distributed monolayer with just few stacking points. Probably

the lack of adsorbed SiO_2 is related to the reduced mobility of large nanoparticles while in suspension at the dipping solution. Additionally, the rinsing steps might be dragging some nanoparticles from the substrate once the 400nm SiO_2 were not homogeneously distributed along the surface.

The $(PDDA/SiO_2$ (400nm) $0.03\%)_{12}$+silane exhibits WCA = 112º ± 5 and SA > 30°, indicating a fully-wetted Wenzel state [88]; after the deposition of $(PDDA/SiO_2$ (22nm) $0.03\%)_3$, the resulting coating is constituted by a non-close packed monolayer of raspberry-like nanoparticles and exhibits a surprisingly WCA = 167° ± 3 and SA < 3°. The wettability of $(PDDA/SiO_2$ (400nm) $0.03\%)_{12}$+silane and $(PDDA/SiO_2$ (400nm+22nm) $0.03\%)_{12+3}$+silane is respectively illustrated on Figure 5.17a-b. The superhydrophobic effect of $(PDDA/SiO_2$ (400nm+22nm) $0.03\%)_{12+3}$+silane coating is shown on Figure 5.17c

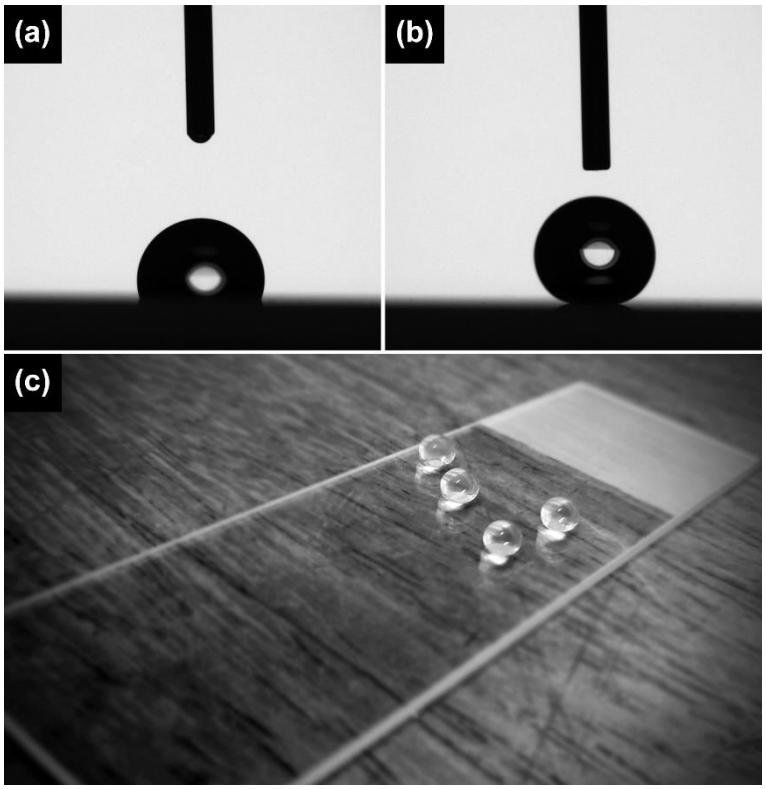

Figure 5.17 - Wettability of (a) $(PDDA/SiO_2$ (400nm) $0.03\%)_{12}$+silane; (b) $(PDDA/SiO_2$ (400nm+22nm) $0.03\%)_{12+3}$+silane; and (c) the superhydrophobic effect of $(PDDA/SiO_2$ (400nm+22nm) $0.03\%)_{12+3}$+silane coating.

Due to their non-close packed structure, the surface asperities for both (PDDA/SiO_2 (400nm) 0.03%)$_{12}$+silane and (PDDA/SiO_2 (400nm+22nm) 0.03%)$_{12+3}$+silane can be considered as clusters of large 400nm SiO_2. Once such nanoparticles are nearly spherical, the surface slope can be related to the local contact angle θ_e, as illustrated in Figure 5.18. In this case, the relative penetration depth (h/R) of a water droplet is given by [101]:

$$\frac{h}{R} = 1 + \cos\theta_e \tag{5.7}$$

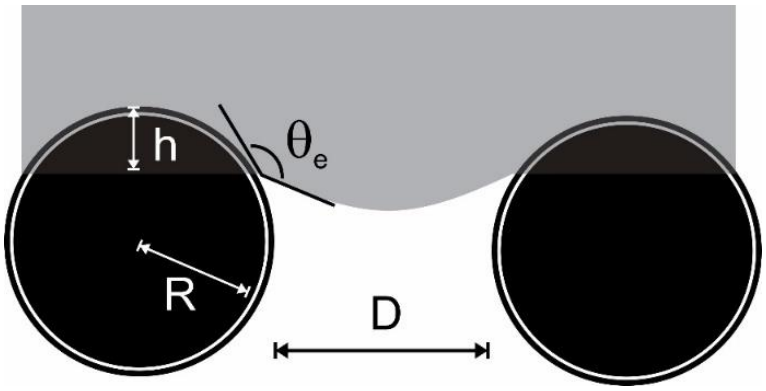

Figure 5.18 - Partial wetting of adjacent SiO_2 clusters.

As a rough estimation, θ_e values can be once more extracted from Table 5.2. For (PDDA/SiO_2 (400nm) 0.03%)$_{12}$+silane constituted exclusively by smooth nanoparticles, $\theta_e \sim 103°$ then $h/R \sim 0.8$. On the other hand, for (PDDA/SiO_2 (400nm+22nm) 0.03%)$_{12+3}$+silane prepared using raspberry-like nanoparticles, $\theta_e \sim 128°$ and $h/R \sim 0.4$. One attentive reader will promptly infer that, for the last one, the solid-liquid-gas contact line is predicted to have a low penetration depth, favoring the Cassie-Baxter state [9] and superhydrophobicity.

Physically speaking, the main force that opposes the infusion of water into the asperities is the *capillary force*, given by the product of the perimeter of the solid-liquid contact line around one cluster of SiO_2 and the vertical component of the liquid surface tension [118–120]. The superhydrophobicity is manifested when the capillary pressure overcomes other pressures which favor the water infusion, i.e. hydrostatic, Laplace and impact pressures [121–124].

Therefore, for (PDDA/SiO_2 (400nm) 0.03%)$_{12}$+silane, probably the capillary pressure is not strong enough to overcome the sum of the opposite pressures, leading to the Wenzel state [88]. On the other hand, the presence of small nanoparticles in (PDDA/SiO_2 (400nm+22nm) 0.03%)$_{12+3}$+silane might have increased the capillary pressure by increasing the local contact angle to $\theta_e \sim 128°$ and, as predicted by Equation (5.7), now it is possible to stabilize the solid-liquid-air interface. Additionally, the 22nm SiO_2 might also be significantly contributing to the pinning effect of the solid-liquid-air contact line due to their small curvature radius [125–128], favoring the Cassie-Baxter regime [9] and, consequently, the superhydrophobic effect.

5.4 Raspberry-like SiO_2 nanoparticles: an elegant spin-off

At this point, there is no doubt that hierarchical structures, such as raspberry-like morphology are a suitable alternative for the preparation of non-wetting surfaces. However, despite its functionality, LbL route is too much time consuming since it requires multiple steps. Additionally, as earlier discussed, assembly cycles are invariable followed by intrinsic defects.

In this context, the usage of pre-prepared raspberry-like nanoparticles potentially improves the speed of the overall process, once two-level hierarchical structures can be readily obtained by a single deposition step. Therefore, as an elegant spin-off developed in partnership with Complex Materials group at ETH Zürich, a step-by-step method to control the surface geometry of SiO_2 was proposed where the parametrization of key variables is the heart (and the most valuable result) of the following discussion.

5.4.1 Strategy and approach

In order to keep the chemical and, especially, the dimensional coherence, raspberry-like SiO_2 nanoparticles were prepared from large 400nm SiO_2 cores synthetized by Stöber process [65] covered by small berries constituted by 22nm LUDOX® TM-40 SiO_2 nanoparticles. The fabrication of raspberry-like

nanoparticles was based on the electrostatic adsorption of negatively charged berries onto the positively charged cores as schematically illustrated by Figure 5.19.

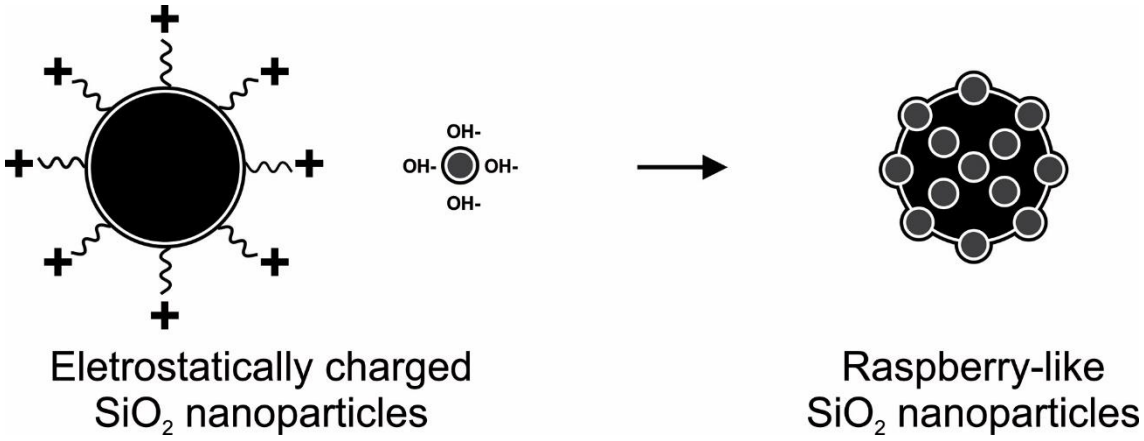

Figure 5.19 - Schematic illustration of the preparation procedure of raspberry-like SiO_2 nanoparticles.

Even though such strategy was previously reported on literature [129–131], there is a lack of technical information explaining how the process should be conducted. In other words, as far as we know, there is no systematic study describing the fundamental parameters of the preparation of raspberry-like SiO_2 nanoparticles; therefore, a robust and reproducible methodology should be proposed from the sketch.

Essentially, some basic principles should be considered while using the electrostatic absorption approach: the process is totally conducted in aqueous solution; every component of the system needs to be electrostatically charged; surface charge is inverted in each adsorption step and flocculation should be avoided. Therefore, zeta potential shows itself as a powerful decision-maker tool.

5.4.2 The positively charged core: 400nm SiO_2

Every adsorption step is followed by an inversion of the electrostatic charge. In this case, surface modification of negatively charged 400nm SiO_2 were

performed with PDDA. Among several possibilities, the PDDA was carefully chosen since it is a strong polycation; thus, the degree of dissociation of its ionic groups is nearly pH-independent [74]. At this point, one can promptly realize that such feature is very useful since there is no pH-range limitation in which PDDA can be employed. Concerning the stability window of 400nm SiO_2 (Figure 5.2) and the PDDA pH dissociation independence, pH ~ 9.0 was fixed.

The surface modification of 400nm SiO_2 were carried out by batch technique using a similar procedure described by Phan et al. [132]. Aqueous 400nm SiO_2 suspension and PDDA solution were prepared and their concentration and volume ratio employed per batch are expressed in Table 5.5.

Table 5.5 - Concentration and volume ratio of the solution and suspension employed in the surface modification of 400nm SiO_2

Component	Concentration (wt%)	Volume ratio (a:b)
[(a)]400nm SiO_2	0.5	1:2
[(b)]PDDA	1.0	

The process was conducted by the dropwise addition of 400nm SiO_2 to PDDA under vigorous stirring for 2h. From our experiments, it is recommended to follow the described mixture protocol to minimize the *bridging effect*. The obtained suspension was centrifuged at 10000 RPM, washed/dispersed 3 times in water and dried in vacuum overnight at room temperature. The surface charge and the stability of 400nm SiO_2-coated aqueous suspension was evaluated by zeta potential over a wide pH range as shown in Figure 5.20.

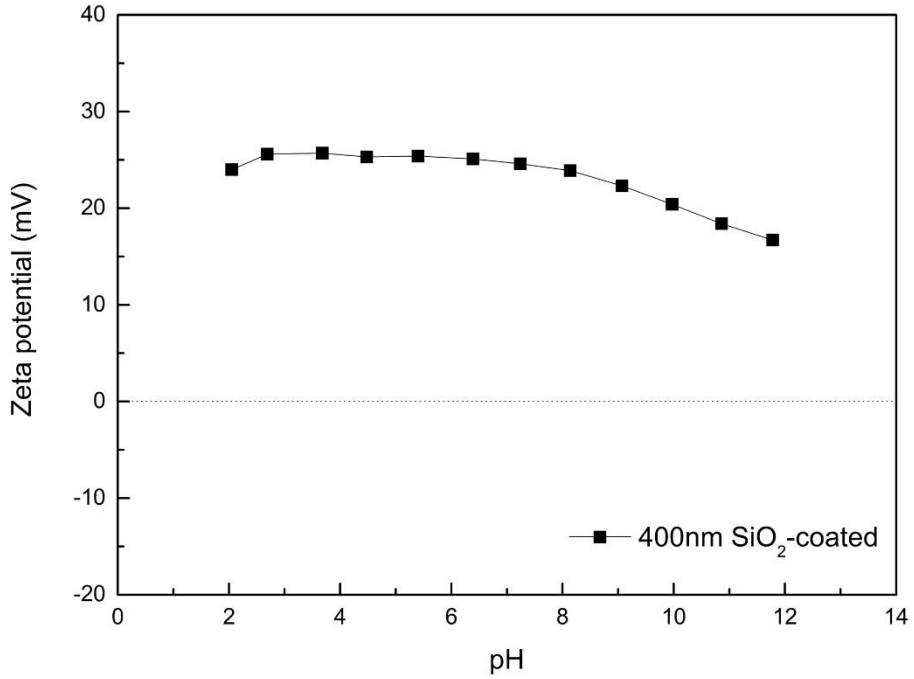

Figure 5.20 - Zeta potential of 400nm SiO_2-coated.

From Figure 5.20, PDDA molecules were successfully adsorbed on 400nm SiO_2 and the obtained nanoparticles are highly positive due to the presence of cationic ammonium groups. The positive ʒ value of 400nm SiO_2-coated is basically constant in the entire pH range. It is not necessary to mention that such feature is more than welcome and provides versatility for the system manipulation.

5.4.3 The negatively charged berries: 22nm SiO_2

Since it was demonstrated that the positive charge of 400nm SiO_2-coated is pH-independent, it becomes necessary to determine the working window for the small berries. As earlier discussed, 22nm SiO_2 have a negative character in a wide pH range. However, in a similar strategy employed for 400nm SiO_2, the criteria is the colloidal stability. From Figure 5.2, stable 22nm SiO_2 suspensions can be prepared above pH 7.5. Therefore, for sake of simplicity, pH ~ 9.0 was fixed again.

In principle, the morphology of raspberry-like nanoparticles can be related to the number of *small berries* assembled on the *core*. Assuming a close-packed monolayered coverage, the maximum theoretical number of small particles N_{max} on a single large particle is geometrically calculated by Equation (5.8) [133].

$$N_{max} = \frac{2\pi}{\sqrt{3}}\left[1 + \left(\frac{R}{r}\right)\right]^2 \quad (5.8)$$

where r and R are, respectively, the radii of small and large nanoparticles.

The preparation of SiO_2 raspberry-like morphology were, once more, carried out by batch technique. 22nm SiO_2 and 400nm SiO_2-coated aqueous suspensions were prepared and the pH adjusted to 9.0. Posteriorly, 22nm SiO_2 was dropwise added to 400nm SiO_2-coated during two steps of 30 min of vigorous stirring intercalated by an ultra-sonication step of 10 min. The obtained suspension was centrifuged at 10000 RPM, washed/dispersed 3 times in water and dried in vacuum overnight at room temperature.

The estimation of N_{max} value was performed considering that both differently-sized nanoparticles are monodispersed and amorphous (i.e. ρ ~ 2.2 g/cm³ [134]). As an attempt to control the surface coverage of the SiO_2 raspberry-like nanoparticles, different multipliers were applied to the theoretical N_{max} value. The N_{max} multipliers, as well the respective concentration and volume ratio of the suspensions employed in each batch, are expressed in Table 5.6. SEM micrographs of the smooth 400nm SiO_2, Rb-1X, Rb-10X and Rb-100X can be observed in Figure 5.21.

Table 5.6 - N_{max} multiplier, concentration and volume ratio of the suspensions employed in the preparation of SiO_2 raspberry-like nanoparticles

Composition	N_{max} multiplier	[a]22nm SiO_2 Concentration (wt%)	[b]400nm SiO_2-coated Concentration (wt%)	Volume ratio (a:b)
Rb-1X	1 X	0.04	0.1	
Rb-10X	10 X	0.4	0.1	1:1
Rb-100X	100 X	4	0.1	

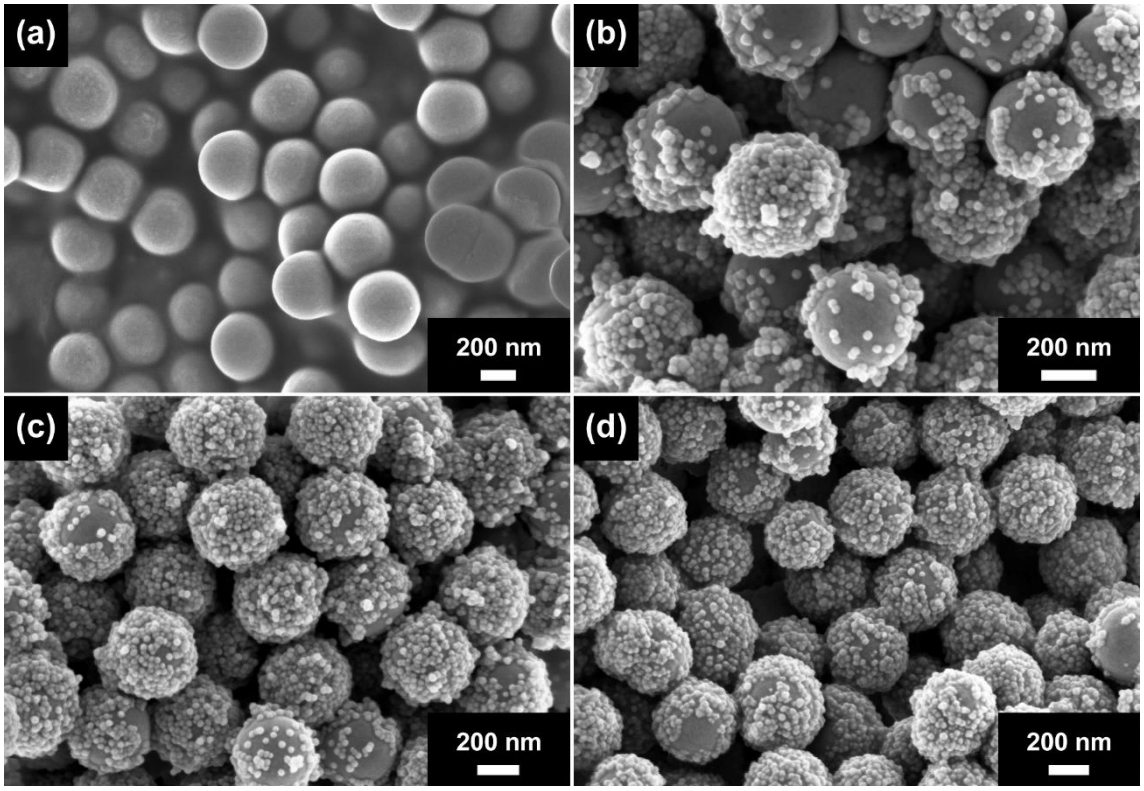

Figure 5.21 - SEM micrographs of (a) 400nm SiO_2; (b) Rb-1X; (c) Rb-10X; and (d) Rb-100X.

According to Figure 5.21, employing excess of small *berries* is mandatory for enhanced homogeneity of raspberry-like SiO_2 once the efficiency of the process is never 100%. However, interestingly we must say, working with lacking small nanoparticles lead to a non-homogeneous structure where some particles are highly covered and other are still almost *bald*. Since the adsorption process

is stochastic, increasing the concentration of small nanoparticles might improve the coverage ratio; nonetheless it is important to mention that, even for highly concentrated 22nm SiO_2 suspensions (i.e. Rb-100X), the coverage will never be perfect, and a large number of defects and non-homogeneities should always be expected.

5.5 *Water-repellent raspberry-like SiO_2*

As the reader probably realized, the preparation of self-supporting raspberry-like SiO_2 open up a world of possibilities once the process is *substrate-free*. In other words, after the proper chemical modification, any surface covered with such nanoparticles can potentially exhibit superhydrophobicity. However, it is not necessary to mention that, in several situations, chemical modification might not be a suitable (or even feasible) task.

Throughout this study, it has been demonstrated and extensively discussed that the key-factor for the superhydrophobic effect is the synergy between hierarchical roughness, here provided by the raspberry-like morphology, and low surface energy. Therefore, it can be inferred that if the nanoparticles intrinsically exhibit low surface energy, superhydrophobicity should naturally be manifested without posterior treatments. So, as a new approach, it was proposed that chemical modification should be directly performed on the raspberry-like SiO_2.

In this way, the chemical modification of Rb-100X was performed according the same procedure described for the coatings. The nanoparticles were dispersed in a 0.25 wt% trichlorododecylsilane solution in chloroform for 1h. After the hydrophobization process, the suspension was washed/re-dispersed in chloroform and centrifuged at 10000 RPM several times in order to remove the non-reacted silane. The remaining powder were dried in vacuum overnight at room temperature. The morphology of Rb-100x+silane as well its water-repellent effect is shown in Figure 5.22.

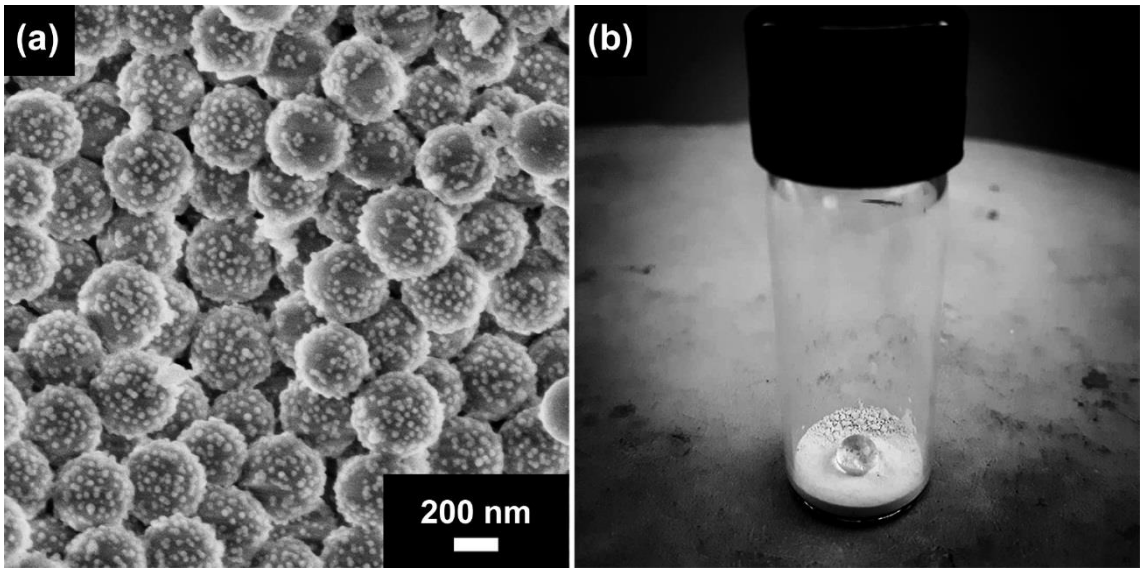

Figure 5.22 - (a) SEM micrograph of Rb-100X+silane; and (b) a spherical water droplet suspended on Rb-100X+silane in powder form.

From Figure 5.22a it is possible to observe that the chemical modification did not destroy the raspberry-like morphology of Rb-100x. On the other hand, by a simple comparison between Figure 5.21d and Figure 5.22a, one could argue that the additional washing/re-dispersing cycles might have partially removed the small “berries”. Naturally it is a plausible possibility, however such kind of comparison should be avoided since defects in the coverage are a side-effect of every adsorption process and homogeneity cannot be guaranteed at any stage; additionally, the entire process is performed in batches, so variations in the nanoparticle size or coverage degree should be expected. Figure 5.22b exhibits the extreme water-repellency of Rb-100x+silane. Due to technical limitations, unfortunately it is not possible to measure the wetting properties such as WCA and SA. Nevertheless, the spherical water droplet easily rolls-off along the surface, characterizing a very low CA hysteresis and providing strong evidences that the powder is, indeed, superhydrophobic.

Here, I would like to thank the reader for following me on this discussion concerning some concepts of superwettability. Additionally, I am pleased to introduce this white powder that can potentially be employed in the preparation

of superhydrophobic surfaces, bringing to life the phenomenon so-called *Lotus effect*.

6 CONCLUSIONS

(i) Despite the importance of superficial roughness, the primary mechanism governing wetting behavior of hydrophilic SiO_2-based multilayer films seems to be the rapid liquid infiltration (nanowicking) into the porous structure. It was found that concentration of dipping suspension and nanoparticle size are closely related to thickness of the multilayer coatings. However, wetting behavior might not to be mainly governed by thickness, as usually reported on literature. At least for the studied system, homogeneity of coatings seems to be the main criteria for superhydrophilicity. In other words, if a uniform structure is obtained, superhydrophilic behavior is observed; notwithstanding, counterintuitively we must admit, further increments in coatings thickness were not followed by respective enhancements on wetting performance.

SEM micrographs suggest the existence of a minimum concentration of SiO_2 in dipping solutions required to produce homogeneous PDDA/SiO_2 coatings via LbL deposition. For the studied system, such hypothetical value is laid between 0.01 wt% and 0.03 wt% for both 7nm and 22nm SiO_2. Since it is supposed that superhydrophilicity is exclusively manifested in homogeneous coatings, the absence of such phenomena in (PDDA/SiO_2 (7nm) 0.01%)$_{15}$ and (PDDA/ SiO_2 (22nm) 0.01%)$_{15}$ might be attributed to the several defects observed along their surface. Such non-homogeneities are probably resulted from the shortage of nanoparticles during the assembling process. As an additional feature, it was observed that several compositions exhibited superior visible light transmittance compared to the uncoated glass. Such interesting effect was attributed to AR properties induced by nanoporosity of the coatings.

(ii) The combination of hierarchical roughness and low surface energy might be a necessary, but not a sufficient condition for superhydrophobicity and the key parameter seems to be the shape of the surface asperities. Hierarchical topographies were prepared by layer-by-layer technique employing two different strategies. As an intrinsic feature of the LbL assembly of the studied system, the local surface slopes of random roughened (PDDA/SiO_2 (22nm) 0.03%)$_n$+silane are almost unaffected by number of deposited bilayers and always lower than the estimated critical value Φ_{crit} required for the stabilization of the solid-liquid-air

interphase. Therefore, wettability of the random roughness surfaces is exclusively controlled by the nanoroughness and, even for high n values, superhydrophobicity is unlikely for this system. As a consequence, a fully wetted Wenzel state is invariably manifested.

Due to their non-closed packed structure, surface asperities of (PDDA/SiO_2 (400nm) 0.03%)$_{12}$+silane and (PDDA/SiO_2 (400nm+22nm) 0.03%)$_{12+3}$+silane can be seen as clusters of large nanospheres; therefore, the local surface slopes can be related to the local contact angle θ_e and the relative penetration depth (h/R) is easily estimated. Since h/R is inversely proportional to θ_e, the presence of small nanoparticles was mandatory for successfully stabilize the solid-liquid-air interface of PDDA/SiO_2 (400nm+22nm) 0.03%)$_{12+3}$+silane. It is proposed that 22nm SiO_2 increases the local contact angle, resulting in a higher capillary pressure which avoids the deep penetration of water into the surface asperities. Additionally, the nanoroughness might also play an important role in the pinning effect of the solid-liquid-air contact line.

(iii) Raspberry-like SiO_2 can be readily prepared through the electrostatic adsorption of negatively charged *berries* onto positively charged *cores*. The employed strategy is based on the control of surface charge of nanoparticles in each adsorption step. Here, such control was performed by zeta potential analysis. Coating inorganic nanoparticles with strong polyelectrolytes seems to be a suitable approach to manipulate their surface charge, opening possibilities not only for raspberry-like geometry, but also for the preparation of diversified hierarchical structures.

(iv) Chemical modification of raspberry-like SiO_2 results in a white powder that can potentially be employed in the preparation of superhydrophobic surfaces, showing itself as a promising *kick-start* for an entirely new concept.

7 REFERENCES

[1] Su, B.; Tian, Y.; Jiang, L. Bioinspired Interfaces with Superwettability: From Materials to Chemistry. *J. Am. Chem. Soc.* **2016**, *6*, 1727–1748, doi:10.1021/jacs.5b12728.

[2] Wang, S.; Liu, K.; Yao, X.; Jiang, L. Bioinspired Surfaces with Superwettability: New Insight on Theory, Design, and Applications. *Chem. Rev.* **2015**, *16*, 8230–8293, doi:10.1021/cr400083y.

[3] Liu, K.; Cao, M.; Fujishima, A.; Jiang, L. Bio-Inspired Titanium Dioxide Materials with Special Wettability and Their Applications. *Chem. Rev.* **2014**, *19*, 10044–10094, doi:10.1021/cr4006796.

[4] Young, T. III. An essay on the cohesion of fluids. *Philos. Trans. R. Soc. London* **1805**, *2*, 65–87, doi:10.1098/rstl.1805.0005.

[5] Langmuir, I. The mechanism of the surface phenomena of flotation. *Trans. Faraday Soc.* **1920**, *June*, 62, doi:10.1039/tf9201500062.

[6] Drelich, J.; Chibowski, E.; Meng, D.D.; Terpilowski, K. Hydrophilic and superhydrophilic surfaces and materials. *Soft Matter* **2011**, *21*, 9804, doi:10.1039/c1sm05849e.

[7] Liu, M.; Wang, S.; Jiang, L. Nature-inspired superwettability systems. *Nat. Rev. Mater.* **2017**, *7*, 17036, doi:10.1038/natrevmats.2017.36.

[8] Wenzel, R.N. RESISTANCE OF SOLID SURFACES TO WETTING BY WATER. *Ind. Eng. Chem.* **1936**, *8*, 988–994, doi:10.1021/ie50320a024.

[9] Cassie, A.B.D.; Baxter, S. Wettability of porous surfaces. *Trans. Faraday Soc.* **1944**, *5*, 546, doi:10.1039/tf9444000546.

[10] Barthlott, W.; Neinhuis, C. Purity of the sacred lotus, or escape from contamination in biological surfaces. *Planta* **1997**, *1*, 1–8, doi:10.1007/s004250050096.

[11] Feng, L.; Li, S.; Li, Y.; Li, H.; Zhang, L.; Zhai, J.; Song, Y.; Liu, B.; Jiang, L.; Zhu, D. Super-Hydrophobic Surfaces: From Natural to Artificial. *Adv. Mater.* **2002**, *24*, 1857–1860, doi:10.1002/adma.200290020.

[12] Drelich, J.; Chibowski, E. Superhydrophilic and Superwetting Surfaces: Definition and Mechanisms of Control. *Langmuir* **2010**, *24*, 18621–18623, doi:10.1021/la1039893.

[13] Dong, H.; Ye, P.; Zhong, M.; Pietrasik, J.; Drumright, R.; Matyjaszewski, K. Superhydrophilic Surfaces via Polymer−SiO 2 Nanocomposites. *Langmuir* **2010**, *19*, 15567–15573, doi:10.1021/la102145s.

[14] Feng, X.J.; Jiang, L. Design and Creation of Superwetting/Antiwetting Surfaces. *Adv. Mater.* **2006**, *23*, 3063–3078, doi:10.1002/adma.200501961.

[15] Zhang, X.-T.; Sato, O.; Taguchi, M.; Einaga, Y.; Murakami, T.; Fujishima, A. Self-Cleaning Particle Coating with Antireflection Properties. *Chem. Mater.* **2005**, *3*, 696–700, doi:10.1021/cm0484201.

[16] Miyauchi, M.; Nakajima, A.; Hashimoto, K.; Watanabe, T. A Highly Hydrophilic Thin Film Under 1 μW/cm2 UV Illumination. *Adv. Mater.* **2000**, *24*, 1923–1927, doi:10.1002/1521-4095(200012)12:24<1923::AID-ADMA1923>3.0.CO;2-#.

[17] Sun, R.-D.; Nakajima, A.; Fujishima, A.; Watanabe, T.; Hashimoto, K. Photoinduced Surface Wettability Conversion of ZnO and TiO 2 Thin Films. *J. Phys. Chem. B* **2001**, *10*, 1984–1990, doi:10.1021/jp002525j.

[18] Wang, R.; Hashimoto, K.; Fujishima, A.; Chikuni, M.; Kojima, E.; Kitamura, A.; Shimohigoshi, M.; Watanabe, T. Light-induced amphiphilic surfaces. *Nature* **1997**, *6641*, 431–432, doi:10.1038/41233.

[19] McHale, G.; Shirtcliffe, N.J.; Aqil, S.; Perry, C.C.; Newton, M.I. Topography Driven Spreading. *Phys. Rev. Lett.* **2004**, *3*, 036102, doi:10.1103/PhysRevLett.93.036102.

[20] Shirtcliffe, N.J.; McHale, G.; Newton, M.I.; Perry, C.C.; Roach, P. Porous materials show superhydrophobic to superhydrophilic switching. *Chem. Commun.* **2005**, *25*, 3135, doi:10.1039/b502896e.

[21] Zorba, V.; Chen, X.; Mao, S.S. Superhydrophilic TiO2 surface without photocatalytic activation. *Appl. Phys. Lett.* **2010**, *9*, 093702, doi:10.1063/1.3291667.

[22] Ganjoo, S.; Azimirad, R.; Akhavan, O.; Moshfegh, a Z. Persistent superhydrophilicity of sol–gel derived nanoporous silica thin films. *J. Phys. D. Appl. Phys.* **2009**, *2*, 025302, doi:10.1088/0022-3727/42/2/025302.

[23] Zhao, Y.; Li, M.; Lu, Q.; Shi, Z. Superhydrophobic Polyimide Films with a Hierarchical Topography: Combined Replica Molding and Layer-by-Layer Assembly. *Langmuir* **2008**, *21*, 12651–12657, doi:10.1021/la8024364.

[24] Lopez-Torres, D.; Elosua, C.; Hernaez, M.; Goicoechea, J.; Arregui, F.J. From superhydrophilic to superhydrophobic surfaces by means of polymeric Layer-by-Layer films. *Appl. Surf. Sci.* **2015**, 1081–1086, doi:10.1016/j.apsusc.2015.06.004.

[25] Yokoi, N.; Manabe, K.; Tenjimbayashi, M.; Shiratori, S. Optically Transparent Superhydrophobic Surfaces with Enhanced Mechanical Abrasion Resistance Enabled by Mesh Structure. *ACS Appl. Mater. Interfaces* **2015**, *8*, 4809–4816, doi:10.1021/am508726k.

[26] Castro, L.D.C. de; Larocca, N.M.; Pessan, L.A. Towards the development of superhydrophilic SiO2-based nanoporous coatings: concentration and particle size effect. *Thin Solid Films* **2018**, *September 2017*, 138–144, doi:10.1016/j.tsf.2018.01.045.

[27] Koch, K.; Barthlott, W. Superhydrophobic and superhydrophilic plant surfaces: an inspiration for biomimetic materials. *Philos. Trans. R. Soc. A Math. Phys. Eng. Sci.* **2009**, *1893*, 1487–1509, doi:10.1098/rsta.2009.0022.

[28] Bhushan, B.; Jung, Y.C. Natural and biomimetic artificial surfaces for superhydrophobicity, self-cleaning, low adhesion, and drag reduction. *Prog. Mater. Sci.* **2011**, *1*, 1–108, doi:10.1016/j.pmatsci.2010.04.003.

[29] Berg, J.M.; Eriksson, L.G.T.; Claesson, P.M.; Borve, K.G.N. Three-Component Langmuir-Blodgett Films with a Controllable Degree of Polarity. *Langmuir* **1994**, *4*, 1225–1234, doi:10.1021/la00016a041.

[30] Vogler, E.A. Structure and reactivity of water at biomaterial surfaces. *Adv. Colloid Interface Sci.* **1998**, *1–3*, 69–117, doi:10.1016/S0001-8686(97)00040-7.

[31] Guo, C.; Wang, S.; Liu, H.; Feng, L.; Song, Y.; Jiang, L. Wettability Alteration of Polymer Surfaces Produced by Scraping. *J. Adhes. Sci. Technol.* **2008**, *3–4*, 395–402, doi:10.1163/156856108X304832.

[32] Bico, J.; Marzolin, C.; Quéré, D. Pearl drops. *Europhys. Lett.* **1999**, *2*, 220–226, doi:10.1209/epl/i1999-00548-y.

[33] Han, Z.; Feng, X.; Guo, Z.; Niu, S.; Ren, L. Flourishing Bioinspired Antifogging Materials with Superwettability: Progresses and Challenges. *Adv. Mater.* **2018**, *13*, 1704652, doi:10.1002/adma.201704652.

[34] Wang, S.; Jiang, L. Definition of Superhydrophobic States. *Adv. Mater.* **2007**, *21*, 3423–3424, doi:10.1002/adma.200700934.

[35] Onda, T.; Shibuichi, S.; Satoh, N.; Tsujii, K. Super-Water-Repellent Fractal Surfaces. *Langmuir* **1996**, *9*, 2125–2127, doi:10.1021/la950418o.

[36] Lu, X.; Zhang, C.; Han, Y. Low-Density Polyethylene Superhydrophobic Surface by Control of Its Crystallization Behavior. *Macromol. Rapid Commun.* **2004**, *18*, 1606–1610, doi:10.1002/marc.200400256.

[37] Erbil, H.; Demirel, A.; Avcı, Y.; Mert, O. Transformation of a Simple Plastic into a Superhydrophobic Surface. *Science (80-.).* **2003**, *5611*, 1377–1380, doi:10.1126/science.1078365.

[38] Han, J.T.; Xu, X.; Cho, K. Diverse access to artificial superhydrophobic surfaces using block copolymers. *Langmuir* **2005**, *15*, 6662–6665, doi:10.1021/la051042+.

[39] Li, X.; Chen, G.; Ma, Y.; Feng, L.; Zhao, H.; Jiang, L.; Wang, F. Preparation of a super-hydrophobic poly(vinyl chloride) surface via solvent–nonsolvent coating. *Polymer (Guildf).* **2006**, *2*, 506–509, doi:10.1016/j.polymer.2005.08.097.

[40] Xie, Q.; Xu, J.; Feng, L.; Jiang, L.; Tang, W.; Luo, X.; Han, C.C. Facile Creation of a Super-Amphiphobic Coating Surface with Bionic Microstructure. *Adv. Mater.* **2004**, *4*, 302–305, doi:10.1002/adma.200306281.

[41] Wang, P.; Zhao, T.; Bian, R.; Wang, G.; Liu, H. Robust Superhydrophobic Carbon Nanotube Film with Lotus Leaf Mimetic Multiscale Hierarchical Structures. *ACS Nano* **2017**, *12*, 12385–12391, doi:10.1021/acsnano.7b06371.

[42] Lau, K.K.S.; Bico, J.; Teo, K.B.K.; Chhowalla, M.; Amaratunga, G.A.J.; Milne, W.I.; McKinley, G.H.; Gleason, K.K. Superhydrophobic Carbon Nanotube Forests. *Nano Lett.* **2003**, *12*, 1701–1705, doi:10.1021/nl034704t.

[43] Liu, H.; Feng, L.; Zhai, J.; Jiang, L.; Zhu, D. Reversible Wettability of a Chemical Vapor Deposition Prepared ZnO Film between Superhydrophobicity and Superhydrophilicity. *Langmuir* **2004**, *14*, 5659–5661, doi:10.1021/la036280o.

[44] Jiang, L.; Zhao, Y.; Zhai, J. A Lotus-Leaf-like Superhydrophobic Surface: A Porous Microsphere/Nanofiber Composite Film Prepared by Electrohydrodynamics. *Angew. Chemie Int. Ed.* **2004**, *33*, 4338–4341, doi:10.1002/anie.200460333.

[45] Tuteja, A.; Choi, W.; Mabry, J.M.; McKinley, G.H.; Cohen, R.E. Robust omniphobic surfaces. *Proc. Natl. Acad. Sci.* **2008**, *47*, 18200–18205, doi:10.1073/pnas.0804872105.

[46] Wang, L.; Zhao, Y.; Wang, J.; Hong, X.; Zhai, J.; Jiang, L.; Wang, F. Ultra-fast spreading on superhydrophilic fibrous mesh with nanochannels. *Appl. Surf. Sci.* **2009**, *9*, 4944–4949, doi:10.1016/j.apsusc.2008.12.042.

[47] Tijing, L.D.; Ruelo, M.T.G.; Amarjargal, A.; Pant, H.R.; Park, C.-H.; Kim, D.W.; Kim, C.S. Antibacterial and superhydrophilic electrospun polyurethane nanocomposite fibers containing tourmaline nanoparticles. *Chem. Eng. J.* **2012**, 41–48, doi:10.1016/j.cej.2012.05.005.

[48] Wang, S.; Feng, L.; Jiang, L. One-Step Solution-Immersion Process for the Fabrication of Stable Bionic Superhydrophobic Surfaces. *Adv. Mater.* **2006**, *6*, 767–770, doi:10.1002/adma.200501794.

[49] Iler, R.K. Multilayers of colloidal particles. *J. Colloid Interface Sci.* **1966**, *6*, 569–594, doi:10.1016/0095-8522(66)90018-3.

[50] Decher, G.; Hong, J. Buildup of ultrathin multilayer films by a self-assembly process, 1 consecutive adsorption of anionic and cationic bipolar amphiphiles on charged surfaces. *Makromol. Chemie. Macromol. Symp.* **1991**, *1*, 321–327, doi:10.1002/masy.19910460145.

[51] Decher, G.; Hong, J.D.; Schmitt, J. Buildup of ultrathin multilayer films by a self-assembly process: III. Consecutively alternating adsorption of anionic and cationic polyelectrolytes on charged surfaces. *Thin Solid Films* **1992**, *PART 2*, 831–835, doi:10.1016/0040-6090(92)90417-A.

[52] Zhang, X.; Chen, H.; Zhang, H. Layer-by-layer assembly: from conventional to unconventional methods. *Chem. Commun.* **2007**, *14*, 1395–1405, doi:10.1039/B615590A.

[53] Liu, X.; He, J. Superhydrophilic and Antireflective Properties of Silica Nanoparticle Coatings Fabricated via Layer-by-Layer Assembly and Postcalcination. *J. Phys. Chem. C* **2009**, *1*, 148–152, doi:10.1021/jp808324c.

[54] Zhang, L.; Qiao, Z.-A.; Zheng, M.; Huo, Q.; Sun, J. Rapid and substrate-independent layer-by-layer fabrication of antireflection- and antifogging-integrated coatings. *J. Mater. Chem.* **2010**, *29*, 6125, doi:10.1039/c0jm00792g.

[55] Xu, L.; He, J. Antifogging and antireflection coatings fabricated by integrating solid and mesoporous silica nanoparticles without any post-treatments. *ACS Appl. Mater. Interfaces* **2012**, *6*, 3293–3299, doi:10.1021/am300658e.

[56] Geng, Z.; He, J.; Xu, L. Fabrication of superhydrophilic and antireflective silica coatings on poly(methyl methacrylate) substrates. *Mater. Res. Bull.* **2012**, *6*, 1562–1567, doi:10.1016/j.materresbull.2012.02.029.

[57] Guo, H.; Sun, P.; Liang, Y.; Ma, Y.; Qin, Z.; Cui, S. In-situ fabrication of polyelectrolyte-CSH superhydrophilic coatings via layer-by-layer assembly. *Chem. Eng. J.* **2014**, 198–206, doi:10.1016/j.cej.2014.05.025.

[58] Choi, M.; Xiangde, L.; Park, J.; Choi, D.; Heo, J.; Chang, M.; Lee, C.; Hong, J. Superhydrophilic coatings with intricate nanostructure based on biotic materials for antifogging and antibiofouling applications. *Chem. Eng. J.* **2017**, 463–470, doi:10.1016/j.cej.2016.10.052.

[59] Zhai, L.; Cebeci, F.Ç.; Cohen, R.E.; Rubner, M.F. Stable Superhydrophobic Coatings from Polyelectrolyte Multilayers. *Nano Lett.* **2004**, *7*, 1349–1353, doi:10.1021/nl049463j.

[60] Soeno, T.; Inokuchi, K.; Shiratori, S. Ultra-water-repellent surface: fabrication of complicated structure of SiO2 nanoparticles by electrostatic self-assembled films. *Appl. Surf. Sci.* **2004**, *1–4*, 539–543, doi:10.1016/j.apsusc.2004.06.041.

[61] Zhang, L.; Li, Y.; Sun, J.; Shen, J. Mechanically Stable Antireflection and Antifogging Coatings Fabricated by the Layer-by-Layer Deposition Process and Postcalcination. *Langmuir* **2008**, *19*, 10851–10857, doi:10.1021/la801806r.

[62] Li, Y.; Liu, F.; Sun, J. A facile layer-by-layer deposition process for the fabrication of highly transparent superhydrophobic coatings. *Chem. Commun.* **2009**, *19*, 2730, doi:10.1039/b900804g.

[63] Du, X.; He, J. A Self-Templated Etching Route to Surface-Rough Silica Nanoparticles for Superhydrophobic Coatings. *ACS Appl. Mater. Interfaces* **2011**, *4*, 1269–1276, doi:10.1021/am200079w.

[64] Zhang, C.; Zhang, S.; Gao, P.; Ma, H.; Wei, Q. Superhydrophobic hybrid films prepared from silica nanoparticles and ionic liquids via layer-by-layer self-assembly. *Thin Solid Films* **2014**, *PartA*, 27–32, doi:10.1016/j.tsf.2014.08.045.

[65] Stöber, W.; Fink, A.; Bohn, E. Controlled growth of monodisperse silica spheres in the micron size range. *J. Colloid Interface Sci.* **1968**, *1*, 62–69, doi:10.1016/0021-9797(68)90272-5.

[66] Bell, N.C.; Minelli, C.; Tompkins, J.; Stevens, M.M.; Shard, A.G. Emerging Techniques for Submicrometer Particle Sizing Applied to Stöber Silica. *Langmuir* **2012**, *29*, 10860–10872, doi:10.1021/la301351k.

[67] Bogush, G.H.; Tracy, M.A.; Zukoski, C.F. Preparation of monodisperse silica particles: Control of size and mass fraction. *J. Non. Cryst. Solids* **1988**, *1*, 95–106, doi:10.1016/0022-3093(88)90187-1.

[68] Giesche, H. Synthesis of monodispersed silica powders I. Particle properties and reaction kinetics. *J. Eur. Ceram. Soc.* **1994**, *3*, 189–204, doi:10.1016/0955-2219(94)90087-6.

[69] Kim, J.W.; Kim, L.U.; Kim, C.K. Size Control of Silica Nanoparticles and Their Surface Treatment for Fabrication of Dental Nanocomposites. *Biomacromolecules* **2007**, *1*, 215–222, doi:10.1021/bm060560b.

[70] Stalder, A.F.; Melchior, T.; Müller, M.; Sage, D.; Blu, T.; Unser, M. Low-bond axisymmetric drop shape analysis for surface tension and contact angle measurements of sessile drops. *Colloids Surfaces A Physicochem. Eng. Asp.* **2010**, *1–3*, 72–81, doi:10.1016/j.colsurfa.2010.04.040.

[71] Dubas, S.T.; Schlenoff, J.B. Factors Controlling the Growth of Polyelectrolyte Multilayers. *Macromolecules* **1999**, *24*, 8153–8160, doi:10.1021/ma981927a.

[72] Büscher, K.; Graf, K.; Ahrens, H.; Helm, C.A. Influence of Adsorption Conditions on the Structure of Polyelectrolyte Multilayers. *Langmuir* **2002**, *9*, 3585–3591, doi:10.1021/la011682m.

[73] Choi, J.; Rubner, M.F. Influence of the Degree of Ionization on Weak Polyelectrolyte Multilayer Assembly. *Macromolecules* **2005**, *1*, 116–124, doi:10.1021/ma048596o.

[74] Zhitomirsky, I. Cathodic electrodeposition of ceramic and organoceramic materials. Fundamental aspects. *Adv. Colloid Interface Sci.* **2002**, *1–3*, 279–317, doi:10.1016/S0001-8686(01)00068-9.

[75] Xu, R. Progress in nanoparticles characterization: Sizing and zeta potential measurement. *Particuology* **2008**, *2*, 112–115, doi:10.1016/j.partic.2007.12.002.

[76] Kim, J.; Lawler, D.F. Characteristics of Zeta Potential Distribution in Silica Particles. *Bull. Korean Chem. Soc.* **2005**, *7*, 1083–1089, doi:10.5012/bkcs.2005.26.7.1083.

[77] Antonio Alves Júnior, J.; Baptista Baldo, J. The Behavior of Zeta Potential of Silica Suspensions. *New J. Glas. Ceram.* **2014**, *02*, 29–37, doi:10.4236/njgc.2014.42004.

[78] Bico, J.; Thiele, U.; Quéré, D. Wetting of textured surfaces. *Colloids Surfaces A Physicochem. Eng. Asp.* **2002**, *1–3*, 41–46, doi:10.1016/S0927-7757(02)00061-4.

[79] Cebeci, F.Ç.; Wu, Z.; Zhai, L.; Cohen, R.E.; Rubner, M.F. Nanoporosity-Driven Superhydrophilicity: A Means to Create Multifunctional Antifogging Coatings. *Langmuir* **2006**, *6*, 2856–2862, doi:10.1021/la053182p.

[80] Lvov, Y.; Ariga, K.; Onda, M.; Ichinose, I.; Kunitake, T. Alternate Assembly of Ordered Multilayers of SiO 2 and Other Nanoparticles and Polyions. *Langmuir* **1997**, *23*, 6195–6203, doi:10.1021/la970517x.

[81] Sennerfors, T.; Bogdanovic, G.; Tiberg, F. Formation, Chemical Composition, and Structure of Polyelectrolyte−Nanoparticle Multilayer Films. *Langmuir* **2002**, *16*, 6410–6415, doi:10.1021/la020204o.

[82] Bogdanovic, G.; Sennerfors, T.; Zhmud, B.; Tiberg, F. Formation and Structure of Polyelectrolyte and Nanoparticle Multilayers: Effect of Particle

Characteristics. *J. Colloid Interface Sci.* **2002**, *1*, 44–51, doi:10.1006/jcis.2002.8583.

[83] Chen, P.; Hu, Y.; Wei, C. Preparation of superhydrophilic mesoporous SiO2 thin films. *Appl. Surf. Sci.* **2012**, *10*, 4334–4338, doi:10.1016/j.apsusc.2011.12.109.

[84] Bravo, J.; Zhai, L.; Wu, Z.; Cohen, R.E.; Rubner, M.F. Transparent Superhydrophobic Films Based on Silica Nanoparticles. *Langmuir* **2007**, *13*, 7293–7298, doi:10.1021/la070159q.

[85] Brassard, J.-D.; Sarkar, D.K.; Perron, J. Synthesis of Monodisperse Fluorinated Silica Nanoparticles and Their Superhydrophobic Thin Films. *ACS Appl. Mater. Interfaces* **2011**, *9*, 3583–3588, doi:10.1021/am2007917.

[86] Nimittrakoolchai, O.-U.; Supothina, S. Deposition of organic-based superhydrophobic films for anti-adhesion and self-cleaning applications. *J. Eur. Ceram. Soc.* **2008**, *5*, 947–952, doi:10.1016/j.jeurceramsoc.2007.09.025.

[87] Xu, L.; He, J. Fabrication of Highly Transparent Superhydrophobic Coatings from Hollow Silica Nanoparticles. *Langmuir* **2012**, *19*, 7512–7518, doi:10.1021/la301420p.

[88] Wenzel, R.N. Surface Roughness and Contact Angle. *J. Phys. Colloid Chem.* **1949**, *9*, 1466–1467, doi:10.1021/j150474a015.

[89] Cho, K.L.; Liaw, I.I.; Wu, A.H.F.; Lamb, R.N. Influence of Roughness on a Transparent Superhydrophobic Coating. *J. Phys. Chem. C* **2010**, *25*, 11228–11233, doi:10.1021/jp103479k.

[90] Di Mundo, R.; Bottiglione, F.; Carbone, G. Cassie state robustness of plasma generated randomly nano-rough surfaces. *Appl. Surf. Sci.* **2014**, *1*, 324–332, doi:10.1016/j.apsusc.2014.07.184.

[91] Méndez-Vilas, A.; Donoso, M.G.; González-Carrasco, J.L.; González-Martín, M.L. Looking at the micro-topography of polished and blasted Ti-based biomaterials using atomic force microscopy and contact angle goniometry. *Colloids Surfaces B Biointerfaces* **2006**, *2*, 157–166, doi:10.1016/j.colsurfb.2006.05.002.

[92] Carmo MP.Differential geometry of curves and surfaces, 1st ed.

[93] Gadelmawla, E.S.; Koura, M.M.; Maksoud, T.M.A.; Elewa, I.M.; Soliman, H.H. Roughness parameters. *J. Mater. Process. Technol.* **2002**, *1*, 133–145, doi:10.1016/S0924-0136(02)00060-2.

[94] Bathomarco, R..; Solorzano, G.; Elias, C..; Prioli, R. Atomic force microscopy analysis of different surface treatments of Ti dental implant surfaces. *Appl. Surf. Sci.* **2004**, *1–4*, 29–34, doi:10.1016/j.apsusc.2004.04.007.

[95] Määttänen, A.; Fallarero, A.; Kujala, J.; Ihalainen, P.; Vuorela, P.; Peltonen, J. Printed paper-based arrays as substrates for biofilm formation. *AMB Express* **2014**, *1*, 32, doi:10.1186/s13568-014-0032-0.

[96] Yang, J.; Pi, P.; Wen, X.; Zheng, D.; Xu, M.; Cheng, J.; Yang, Z. A novel method to fabricate superhydrophobic surfaces based on well-defined mulberry-like particles and self-assembly of polydimethylsiloxane. *Appl. Surf. Sci.* **2009**, *6*, 3507–3512, doi:10.1016/j.apsusc.2008.09.092.

[97] Qu, A.; Wen, X.; Pi, P.; Cheng, J.; Yang, Z. Preparation of hybrid film with superhydrophobic surfaces based on irregularly structure by emulsion polymerization. *Appl. Surf. Sci.* **2007**, *24*, 9430–9434, doi:10.1016/j.apsusc.2007.06.002.

[98] Xu, W.; Wang, S.; Hao, L.; Wang, X. Preparation and characterization of trilayer core-shell polysilsesquioxane-fluoroacrylate copolymer composite emulsion particles. *J. Appl. Polym. Sci.* **2017**, *23*, 1–9, doi:10.1002/app.44845.

[99] Possart, W.; Kamusewitz, H. Wetting and scanning force microscopy on rough polymer surfaces: Wenzel's roughness factor and the thermodynamic contact angle. *Appl. Phys. A Mater. Sci. Process.* **2003**, *6*, 899–902, doi:10.1007/s00339-002-1972-9.

[100] Chetwynd, D.G. Slope Measurement in Surface Texture Analysis. *J. Mech. Eng. Sci.* **1978**, *3*, 115–119, doi:10.1243/JMES_JOUR_1978_020_021_02.

[101] Detrich, Á.; Nyári, M.; Volentiru, E.; Hórvölgyi, Z. Estimation of contact angle for hydrophobic silica nanoparticles in their hexagonally ordered layer. *Mater. Chem. Phys.* **2013**, *2–3*, 602–609, doi:10.1016/j.matchemphys.2013.04.013.

[102] Ling, X.Y.; Phang, I.Y.; Vancso, G.J.; Huskens, J.; Reinhoudt, D.N. Stable and Transparent Superhydrophobic Nanoparticle Films. *Langmuir* **2009**, *5*, 3260–3263, doi:10.1021/la8040715.

[103] DETTRE, R.H.; JOHNSON, R.E.Contact Angle Hysteresis, in: Adv Chem Ser, : pp. 136–144 doi:10.1021/ba-1964-0043.ch008.

[104] Yang, C.; Tartaglino, U.; Persson, B.N.J. Nanodroplets on rough hydrophilic and hydrophobic surfaces. *Eur. Phys. J. E* **2008**, *2*, 139–152, doi:10.1140/epje/i2007-10271-7.

[105] Afferrante, L.; Carbone, G. Effect of drop volume and surface statistics on the superhydrophobicity of randomly rough substrates. *J. Phys. Condens. Matter* **2018**, *4*, 045001, doi:10.1088/1361-648X/aaa0f5.

[106] Bottiglione, F.; Carbone, G. Role of Statistical Properties of Randomly Rough Surfaces in Controlling Superhydrophobicity. *Langmuir* **2013**, *2*, 599–609, doi:10.1021/la304072p.

[107] Calvimontes, A. A thermodynamic approach to predict apparent contact angles on microstructures using surface polygonal maps. *Soft Matter* **2014**, *41*, 8308–8323, doi:10.1039/C4SM00789A.

[108] Kota, A.K.; Kwon, G.; Tuteja, A. The design and applications of superomniphobic surfaces. *NPG Asia Mater.* **2014**, *7*, e109–e109, doi:10.1038/am.2014.34.

[109] Sarkar, S.; Patra, S.; Gayathri, N.; Banerjee, S. Effect of self-affine fractal characteristics of surfaces on wetting. *Appl. Phys. Lett.* **2010**, *6*, 063112, doi:10.1063/1.3309690.

[110] Bhushan, B.Surface Roughness Analysis and Measurement Techniques, in: Mod. Tribol. Handb., : pp. 49–119 doi:10.1201/9780849377877.ch2.

[111] Nosonovsky, M.; Bhushan, B. Biologically Inspired Surfaces: Broadening the Scope of Roughness**. *Adv. Funct. Mater.* **2008**, *6*, 843–855, doi:10.1002/adfm.200701195.

[112] Palasantzas, G.; de Hosson, J.T.M. Wetting on rough surfaces. *Acta Mater.* **2001**, *17*, 3533–3538, doi:10.1016/S1359-6454(01)00238-5.

[113] ten Brink, G.H.; Foley, N.; Zwaan, D.; Kooi, B.J.; Palasantzas, G. Roughness controlled superhydrophobicity on single nanometer length scale with

metal nanoparticles. *RSC Adv.* **2015**, *36*, 28696–28702, doi:10.1039/C5RA02348C.

[114] Ming, W.; Wu, D.; van Benthem, R.; de With, G. Superhydrophobic Films from Raspberry-like Particles. *Nano Lett.* **2005**, *11*, 2298–2301, doi:10.1021/nl0517363.

[115] Tsai, H.-J.; Lee, Y.-L. Facile Method to Fabricate Raspberry-like Particulate Films for Superhydrophobic Surfaces. *Langmuir* **2007**, *25*, 12687–12692, doi:10.1021/la702521u.

[116] Zhao, Z.-B.; Zhang, D.-M.; Meng, Y.-F.; Tai, L.; Jiang, Y. One-pot fabrication of fluoride-silica@silica raspberry-like nanoparticles for superhydrophobic coating. *Ceram. Int.* **2016**, *13*, 14601–14608, doi:10.1016/j.ceramint.2016.06.076.

[117] Mammen, L.; Deng, X.; Untch, M.; Vijayshankar, D.; Papadopoulos, P.; Berger, R.; Riccardi, E.; Leroy, F.; Vollmer, D. Effect of Nanoroughness on Highly Hydrophobic and Superhydrophobic Coatings. *Langmuir* **2012**, *42*, 15005–15014, doi:10.1021/la302127y.

[118] Extrand, C.W. Repellency of the Lotus Leaf: Resistance to Water Intrusion under Hydrostatic Pressure. *Langmuir* **2011**, *11*, 6920–6925, doi:10.1021/la201032p.

[119] Nosonovsky, M.; Bhushan, B. Hierarchical roughness optimization for biomimetic superhydrophobic surfaces. *Ultramicroscopy* **2007**, *10–11*, 969–979, doi:10.1016/j.ultramic.2007.04.011.

[120] Ran, C.; Ding, G.; Liu, W.; Deng, Y.; Hou, W. Wetting on Nanoporous Alumina Surface: Transition between Wenzel and Cassie States Controlled by Surface Structure. *Langmuir* **2008**, *18*, 9952–9955, doi:10.1021/la801461j.

[121] Liu, B.; Lange, F.F. Pressure induced transition between superhydrophobic states: Configuration diagrams and effect of surface feature size. *J. Colloid Interface Sci.* **2006**, *2*, 899–909, doi:10.1016/j.jcis.2006.01.025.

[122] Butt, H.-J.; Vollmer, D.; Papadopoulos, P. Super liquid-repellent layers: The smaller the better. *Adv. Colloid Interface Sci.* **2015**, 104–109, doi:10.1016/j.cis.2014.06.002.

[123] Kwak, G.; Lee, M.; Senthil, K.; Yong, K. Impact dynamics of water droplets on chemically modified WOx nanowire arrays. *Appl. Phys. Lett.* **2009**, *15*, 153101, doi:10.1063/1.3244597.

[124] Kwon, H.; Paxson, A.T.; Varanasi, K.K.; Patankar, N.A. Rapid Deceleration-Driven Wetting Transition during Pendant Drop Deposition on Superhydrophobic Surfaces. *Phys. Rev. Lett.* **2011**, *3*, 036102, doi:10.1103/PhysRevLett.106.036102.

[125] Hensel, R.; Finn, A.; Helbig, R.; Killge, S.; Braun, H.-G.; Werner, C. In Situ Experiments To Reveal the Role of Surface Feature Sidewalls in the Cassie–Wenzel Transition. *Langmuir* **2014**, *50*, 15162–15170, doi:10.1021/la503601u.

[126] Extrand, C.W. Modeling of Ultralyophobicity: Suspension of Liquid Drops by a Single Asperity. *Langmuir* **2005**, *23*, 10370–10374, doi:10.1021/la0513050.

[127] Berthier, J.; Loe-Mie, F.; Tran, V.-M.; Schoumacker, S.; Mittler, F.; Marchand, G.; Sarrut, N. On the pinning of interfaces on micropillar edges. *J. Colloid Interface Sci.* **2009**, *1*, 296–303, doi:10.1016/j.jcis.2009.06.007.

[128] Mori, Y.H.; van de Ven, T.G.M.; Mason, S.G. Resistance to spreading of liquids by sharp edged microsteps. *Colloids and Surfaces* **1982**, *1*, 1–15, doi:10.1016/0166-6622(82)80085-1.

[129] Zanini, M.; Hsu, C.-P.; Magrini, T.; Marini, E.; Isa, L. Fabrication of rough colloids by heteroaggregation. *Colloids Surfaces A Physicochem. Eng. Asp.* **2017**, *June*, 116–124, doi:10.1016/j.colsurfa.2017.05.084.

[130] Che, B.H.X.; Yeap, S.P.; Ahmad, A.L.; Lim, J. Layer-by-layer assembly of iron oxide magnetic nanoparticles decorated silica colloid for water remediation. *Chem. Eng. J.* **2014**, *January 2018*, 68–78, doi:10.1016/j.cej.2013.12.095.

[131] Liu, X.; He, J. Hierarchically structured superhydrophilic coatings fabricated by self-assembling raspberry-like silica nanospheres. *J. Colloid Interface Sci.* **2007**, *1*, 341–345, doi:10.1016/j.jcis.2007.05.011.

[132] Pham, T.; Bui, T.; Nguyen, V.; Bui, T.; Tran, T.; Phan, Q.; Pham, T.; Hoang, T. Adsorption of Polyelectrolyte onto Nanosilica Synthesized from Rice Husk: Characteristics, Mechanisms, and Application for Antibiotic Removal. *Polymers (Basel).* **2018**, *2*, 220, doi:10.3390/polym10020220.

[133] Bao, Y.; Li, Q.; Xue, P.; Huang, J.; Wang, J.; Guo, W.; Wu, C. Tailoring the morphology of raspberry-like carbon black/polystyrene composite microspheres for fabricating superhydrophobic surface. *Mater. Res. Bull.* **2011**, *5*, 779–785, doi:10.1016/j.materresbull.2010.09.043.

[134] Zhuravlev, L.T. The surface chemistry of amorphous silica. Zhuravlev model. *Colloids Surfaces A Physicochem. Eng. Asp.* **2000**, *1–3*, 1–38, doi:10.1016/S0927-7757(00)00556-2.

APPENDIX A

A.1 Surface area calculation of (PDDA/SiO_2 (22nm) 0.03%)$_n$+silane

The mathematical definition of surface area (A) is given by [1] :

$$A = \iint \sqrt{1 + \nabla h^2}\, dx\, dy \tag{A.1}$$

where $\nabla h = \sqrt{(\partial h/\partial x)^2 + (\partial h/\partial y)^2}$ is the local surface slope of the surface area. The numerical approximation of Equation A.1 is given by [2] :

$$A = \sum_{j=1}^{M-1} \sum_{i=1}^{N-1} \sqrt{1 + \nabla h_{ij}^2}\ \Delta x\, \Delta y \tag{A.2}$$

where $\nabla h_{ij}^2 = \left(\frac{h(x_{i+1},y_j)-h(x_i,y_j)}{\Delta x}\right)^2 + \left(\frac{h(x_i,y_{j+1})-h(x_i,y_j)}{\Delta y}\right)^2$

From Equation A.2, N and M are, respectively, the numbers of data points in x and y directions; $h(x_i, y_j)$ is the height of the point located at position(x_i, y_j); Δx and Δy are, respectively, the interval length of the data points in x and y direction. As one can realize, ∇h_{ij}^2 utilizes only two consecutive data points for each direction; however, a more reliable computation can be performed by a Lagrange polynomial with additional data points [3]. For six consecutive data points ∇h_{ij}^2 is given by:

$$\begin{aligned}\nabla h_{ij}^2 = \frac{1}{60\Delta x}\big(&-h(x_{i-3},y_j) + 9h(x_{i-2},y_j) - 45h(x_{i-1},y_j)\\ &+ 45h(x_{i+1},y_j) - 9h(x_{i+2},y_j) + h(x_{i+3},y_j)\big)^2\\ &+ \frac{1}{60\Delta y}\big(-h(x_i,y_{j-3}) + 9h(x_i,y_{j-2}) - 45h(x_i,y_{j-1})\\ &+ 45h(x_i,y_{j+1}) - 9h(x_i,y_{j+2}) + h(x_i,y_{j+3})\big)^2\end{aligned} \tag{A.3}$$

Therefore, a routine was written in MATLAB employing this improved computation:

```
function [area,rw] = Areasurfacelagrangian (h,dx);
[lines,colums]=size (h);
k=0;
j=0;
for j=4:(colums-3);
i=0;
for i=4:(lines-3);
k=k+1;
a =  (1/(60*dx)) * ( (h((i+3),j)) -(9*  (h((i+2),j))  )+(45*  (h((i+1),j))  )-(45* (h((i-1),j)) )+(9*  (h((i-2),j)) )-  (h((i-3),j)) );
b =  (1/(60*dx)) * ( (h(i,(j+3))) -(9*  (h(i,(j+2)))  )+(45*  (h(i,(j+1)))  )-(45* (h(i,(j-1))) )+(9*  (h(i,(j-2))) )-  (h(i,(j-3))) );
deltaxy(i-3,j-3) = ( (a^2) + (b^2) )^0.5;
end;
end;
deltaxyquad = deltaxy.^2;
unit = ((deltaxyquad + 1).^0.5).* (dx^2);
sumlinarea = sum(unit);
area = sum  (sumlinarea');
rw = area / ((lines*dx)*(coluns*dx));
```

where h is the matrix $h(x,y)$ from AFM data; and dx is the sampling interval of the respective measurement.

A.2 References

[1] Carmo MP.Differential geometry of curves and surfaces, 1st ed.

[2] Dong, W.P.; Sullivan, P.J.; Stout, K.J. Comprehensive study of parameters for characterising three-dimensional surface topography. *Wear* **1994**, *1–2*, 45–60, doi:10.1016/0043-1648(94)90128-7.

[3] Chetwynd, D.G. Slope Measurement in Surface Texture Analysis. *J. Mech. Eng. Sci.* **1978**, *3*, 115–119, doi:10.1243/JMES_JOUR_1978_020_021_02.